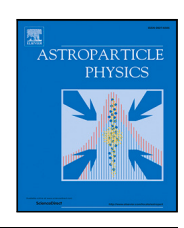
ELSEVIER

Contents lists available at ScienceDirect

#### **Astroparticle Physics**

journal homepage: www.elsevier.com/locate/astropartphys





## The energy spectrum of cosmic rays measured by the Telescope Array using 10 years of fluorescence detector data

```
R.U. Abbasi<sup>1</sup>, Y. Abe<sup>2</sup>, T. Abu-Zayyad<sup>1,3</sup>, M. Allen<sup>3</sup>, Y. Arai<sup>4</sup>, R. Arimura<sup>4</sup>, E. Barcikowski<sup>3</sup>,
J.W. Belz<sup>3</sup>, D.R. Bergman<sup>3,*</sup>, S.A. Blake<sup>3</sup>, I. Buckland<sup>3</sup>, B.G. Cheon<sup>5</sup>, M. Chikawa<sup>6</sup>,
A. Fedvnitch <sup>6,7</sup>, T. Fujii <sup>4,8</sup>, K. Fujisue <sup>6</sup>, K. Fujita <sup>6</sup>, R. Fujiwara <sup>4</sup>, M. Fukushima <sup>6</sup>, G. Furlich <sup>3</sup>,
Z. Gerber<sup>3</sup>, N. Globus<sup>9,a</sup>, W. Hanlon<sup>3</sup>, N. Hayashida<sup>10</sup>, H. He<sup>9</sup>, R. Hibi<sup>2</sup>, K. Hibino<sup>10</sup>,
R. Higuchi<sup>9</sup>, K. Honda<sup>11</sup>, D. Ikeda<sup>10</sup>, N. Inoue<sup>12</sup>, T. Ishii<sup>11</sup>, H. Ito<sup>9</sup>, D. Ivanov<sup>3</sup>, A. Iwasaki<sup>4</sup>,
H.M. Jeong <sup>13</sup>, S. Jeong <sup>13</sup>, C.C.H. Jui <sup>3</sup>, K. Kadota <sup>14</sup>, F. Kakimoto <sup>10</sup>, O. Kalashev <sup>15</sup>,
K. Kasahara <sup>16</sup>, S. Kasami <sup>17</sup>, S. Kawakami <sup>4</sup>, K. Kawata <sup>6</sup>, I. Kharuk <sup>15</sup>, E. Kido <sup>9</sup>, H.B. Kim <sup>5</sup>,
J.H. Kim<sup>3</sup>, J.H. Kim<sup>3,b</sup>, S.W. Kim<sup>13</sup>, Y. Kimura<sup>4</sup>, I. Komae<sup>4</sup>, K. Komori<sup>17</sup>, Y. Kusumori<sup>17</sup>,
M. Kuznetsov <sup>15,18</sup>, Y.J. Kwon <sup>19</sup>, K.H. Lee <sup>5</sup>, M.J. Lee <sup>13</sup>, B. Lubsandorzhiev <sup>15</sup>, J.P. Lundquist <sup>3,20</sup>,
T. Matsuyama <sup>4</sup>, J.A. Matthews <sup>3</sup>, J.N. Matthews <sup>3</sup>, R. Mayta <sup>4</sup>, K. Miyashita <sup>2</sup>, K. Mizuno <sup>2</sup>,
M. Mori <sup>17</sup>, M. Murakami <sup>17</sup>, I. Myers <sup>3</sup>, S. Nagataki <sup>9</sup>, K. Nakai <sup>4</sup>, T. Nakamura <sup>21</sup>, E. Nishio <sup>17</sup>
T. Nonaka <sup>6</sup>, S. Ogio <sup>6</sup>, H. Ohoka <sup>6</sup>, N. Okazaki <sup>6</sup>, Y. Oku <sup>17</sup>, T. Okuda <sup>22</sup>, Y. Omura <sup>4</sup>, M. Onishi <sup>6</sup>,
M. Ono<sup>9</sup>, A. Oshima<sup>23</sup>, H. Oshima<sup>6</sup>, S. Ozawa<sup>24</sup>, I.H. Park<sup>13</sup>, K.Y. Park<sup>5</sup>, M. Potts<sup>3,c</sup>,
M.S. Pshirkov <sup>15,25</sup>, J. Remington <sup>3</sup>, D.C. Rodriguez <sup>3</sup>, C. Rott <sup>3,13</sup>, G.I. Rubtsov <sup>15</sup>, D. Ryu <sup>26</sup>,
H. Sagawa <sup>6</sup>, R. Saito <sup>2</sup>, N. Sakaki <sup>6</sup>, T. Sako <sup>6</sup>, N. Sakurai <sup>4</sup>, D. Sato <sup>2</sup>, K. Sato <sup>4</sup>, S. Sato <sup>17</sup>,
K. Sekino <sup>6</sup>, P.D. Shah <sup>3</sup>, N. Shibata <sup>17</sup>, T. Shibata <sup>6</sup>, J. Shikita <sup>4</sup>, H. Shimodaira <sup>6</sup>, B.K. Shin <sup>26</sup>,
H.S. Shin <sup>6</sup>, D. Shinto <sup>17</sup>, J.D. Smith <sup>3</sup>, P. Sokolsky <sup>3</sup>, B.T. Stokes <sup>3</sup>, T.A. Stroman <sup>3</sup>, Y. Takagi <sup>17</sup>,
K. Takahashi <sup>6</sup>, M. Takamura <sup>27</sup>, M. Takeda <sup>6</sup>, R. Takeishi <sup>6</sup>, A. Taketa <sup>28</sup>, M. Takita <sup>6</sup>,
Y. Tameda <sup>17</sup>, K. Tanaka <sup>29</sup>, M. Tanaka <sup>30</sup>, S.B. Thomas <sup>3</sup>, G.B. Thomson <sup>3</sup>, P. Tinyakov <sup>15,18</sup>, I. Tkachev <sup>15</sup>, H. Tokuno <sup>31</sup>, T. Tomida <sup>2</sup>, S. Troitsky <sup>15</sup>, R. Tsuda <sup>4</sup>, Y. Tsunesada <sup>4,8</sup>, S. Udo <sup>10</sup>,
F. Urban <sup>32</sup>, I.A. Vaiman <sup>15</sup>, D. Warren <sup>9</sup>, T. Wong <sup>3</sup>, K. Yamazaki <sup>23</sup>, K. Yashiro <sup>27</sup>, F. Yoshida <sup>17</sup>.
Y. Zhezher <sup>6,15</sup>, Z. Zundel <sup>3</sup>
```

<sup>&</sup>lt;sup>1</sup> Department of Physics, Loyola University Chicago, Chicago, Illinois 60660, USA

<sup>&</sup>lt;sup>2</sup> Academic Assembly School of Science and Technology Institute of Engineering, Shinshu University, Nagano, Nagano 380-8554, Japan

<sup>&</sup>lt;sup>3</sup> High Energy Astrophysics Institute and Department of Physics and Astronomy, University of Utah, Salt Lake City, Utah 84112-0830, USA

<sup>&</sup>lt;sup>4</sup> Graduate School of Science, Osaka Metropolitan University, Sugimoto, Sumiyoshi, Osaka 558-8585, Japan

<sup>&</sup>lt;sup>5</sup> Department of Physics and The Research Institute of Natural Science, Hanyang University, Seongdong-gu, Seoul 426-791, Korea

<sup>&</sup>lt;sup>6</sup> Institute for Cosmic Ray Research, University of Tokyo, Kashiwa, Chiba 277-8582, Japan

<sup>&</sup>lt;sup>7</sup> Institute of Physics, Academia Sinica, Taipei City 115201, Taiwan

<sup>&</sup>lt;sup>8</sup> Nambu Yoichiro Institute of Theoretical and Experimental Physics, Osaka Metropolitan University, Sugimoto, Sumiyoshi, Osaka 558-8585, Japan

<sup>9</sup> Astrophysical Big Bang Laboratory, RIKEN, Wako, Saitama 351-0198, Japan

<sup>10</sup> Faculty of Engineering, Kanagawa University, Yokohama, Kanagawa 221-8686, Japan

<sup>11</sup> Interdisciplinary Graduate School of Medicine and Engineering, University of Yamanashi, Kofu, Yamanashi 400-8511, Japan

<sup>12</sup> The Graduate School of Science and Engineering, Saitama University, Saitama, Saitama 338-8570, Japan

<sup>&</sup>lt;sup>13</sup> Department of Physics, SungKyunKwan University, Jang-an-gu, Suwon 16419, Korea

<sup>&</sup>lt;sup>14</sup> Department of Physics, Tokyo City University, Setagaya-ku, Tokyo 158-8557, Japan

<sup>&</sup>lt;sup>15</sup> Institute for Nuclear Research of the Russian Academy of Sciences, Moscow 117312, Russia

 $<sup>^{</sup>st}$  Corresponding author.

E-mail address: bergman@physics.utah.edu (D.R. Bergman).

<sup>&</sup>lt;sup>a</sup> Presently at: University of California - Santa Cruz.

<sup>&</sup>lt;sup>b</sup> Presently at: Argonne National Laboratory, Physics Division, Lemont, Illinois, 60439, USA.

<sup>&</sup>lt;sup>c</sup> Presently at: Georgia Institute of Technology, Physics Department, Atlanta, Georgia 30332, USA.

- <sup>16</sup> Faculty of Systems Engineering and Science, Shibaura Institute of Technology, Minato-ku, Tokyo 337-8570, Japan
- <sup>17</sup> Graduate School of Engineering, Osaka Electro-Communication University, Neyagawa-shi, Osaka 572-8530, Japan
- <sup>18</sup> Service de Physique Théorique, Université Libre de Bruxelles, Brussels 1050, Belgium
- <sup>19</sup> Department of Physics, Yonsei University, Seodaemun-gu, Seoul 120-749, Korea
- <sup>20</sup> Center for Astrophysics and Cosmology, University of Nova Gorica, Nova Gorica 5297, Slovenia
- <sup>21</sup> Faculty of Science, Kochi University, Kochi, Kochi 780-8520, Japan
- <sup>22</sup> Department of Physical Sciences, Ritsumeikan University, Kusatsu, Shiga 525-8577, Japan
- <sup>23</sup> College of Science and Engineering, Chubu University, Kasugai, Aichi 487-8501, Japan
- <sup>24</sup> Quantum ICT Advanced Development Center, National Institute for Information and Communications Technology, Koganei, Tokyo 184-8795, Japan
- <sup>25</sup> Sternberg Astronomical Institute, Moscow M.V. Lomonosov State University, Moscow, 119991, Russia
- <sup>26</sup> Department of Physics, School of Natural Sciences, Ulsan National Institute of Science and Technology, UNIST-gil, Ulsan 689-798, Korea
- <sup>27</sup> Department of Physics, Tokyo University of Science, Noda, Chiba 162-8601, Japan
- <sup>28</sup> Earthquake Research Institute, University of Tokyo, Bunkyo-ku, Tokyo 277-8582, Japan
- <sup>29</sup> Graduate School of Information Sciences, Hiroshima City University, Hiroshima, Hiroshima 731-3194, Japan
- 30 Institute of Particle and Nuclear Studies, KEK, Tsukuba, Ibaraki 305-0801, Japan
- <sup>31</sup> Graduate School of Science and Engineering, Tokyo Institute of Technology, Meguro, Tokyo 152-8550, Japan
- 32 CEICO, Institute of Physics, Czech Academy of Sciences, Prague 182 21, Czech Republic

#### ARTICLE INFO

# Keywords: Ultra-high energy cosmic rays Telescope array experiment Cosmic ray energy spectrum Spectral features Monocular reconstruction GZK suppression

#### ABSTRACT

The Telescope Array (TA) Cosmic Ray Observatory is the largest cosmic ray detector in the northern hemisphere. TA was built to study ultra-high-energy cosmic rays (UHECRs), cosmic rays with energies above 10<sup>18</sup> eV. TA is a hybrid detector, employing two distinct detection methods: a surface detector array and a set of fluorescence telescopes. We will present a measurement of the cosmic ray energy spectrum for energies above 10<sup>17.5</sup> eV using only the fluorescence telescopes. A novel weather classification scheme using machine learning was used to select data parts with good weather to ensure the quality of the fluorescence data. The data from the Black Rock Mesa (BRM) and Long Ridge (LR) fluorescence telescope sites were analyzed separately in monocular mode, with the calculated fluxes combined into a single spectrum. The 10-year monocular combined cosmic ray energy spectrum is observed to be in excellent agreement with previous measurements from the northern hemisphere. We present fits of the combined spectrum to a series of broken power law models. The thrice-broken power law was observed to be the best fit considering the Poisson deviance per degrees of freedom. The three breaks suggest an additional feature of the spectrum between the previously observed Ankle feature at 10<sup>18.7</sup> eV and the GZK suppression at 10<sup>19.8</sup> eV.

#### 1. Introduction

Ultra-high energy cosmic rays (UHECRs) are the highest energy particles ever observed, with energies up to at least 50 Joules in a single nucleus [1]. The origins of these particles remains undetermined to this day. Whatever the origin of UHECRs, the distances over which UHECRs can propagate through the universe is severely limited for UHECRs with energies above about 57 EeV. This limiting of propagation distance imposes a horizon beyond which we do not expect to be able to see UHECRs above 57 EeV. This will lead to a drastic reduction in the flux of UHECRs above a given energy. This expected reduction in flux could also be caused by the maximum energy produced by sources of UHECRs, an ambiguity that is difficult to remove. The reduction in the allowed propagation distances can be either due to interactions of the cosmic ray protons with the cosmic microwave background radiation (CMBR), an effect known as the GZK Cutoff after the papers by Greisen [2] and Zatsepin and Kuzmin [3] published shortly after the discovery of the CMBR, or due to the photo-dissociation of heavier nuclei on a similar length scale. The Telescope Array (TA) observatory is the largest cosmic ray detector operating in the northern hemisphere designed to detect UHECRs [4]. It was designed by combining fluorescence detectors designed by the High Resolution Fly's Eye (HiRes) Experiment [5] with a surface detector array developed by the Akeno Giant Air Shower Array (AGASA) [6]. One of TA's predecessors, HiRes, was the first cosmic ray observatory to confirm the existence of the suppression of cosmic rays [7] at the highest level known as the GZK suppression [2,3]. Follow-up measurements with the Pierre Auger Observatory (Auger) [8] and the TA Surface Detector (SD) array [9] also observe a suppression in the cosmic ray flux at the highest energies. The most recent measurement of the UHECR energy flux spectrum by Auger [10,11] has observed a new feature in the spectrum, a softening of the spectrum at a factor of about three below the high

energy suppression. The Auger measurements also do not support the interpretation of the high-energy break as being due to propagation of protons [12], and so it may not be literally the GZK suppression. We will refer to the GZK suppression as the high-energy suppression for most of this paper.

TA has passed 11 years of operation. As a followup to the previous TA FD monocular measurements with 3.5 years [13] and 7.5 years [14] and the latest measurement made by the TA SDs [15], we present a spectrum calculation using 10 years of reconstructed events from the Black Rock (BR) and Long Ridge (LR) FD stations in monocular mode. While the FDs operate with 11% duty cycle and thus have fewer event statistics compared to the roughly 100% duty-cycle of the SDs, the FDs observe the longitudinal development of the Extensive Air Showers (EAS) and have a smaller hadronic model dependency for event reconstruction. The only hadronic-model dependence is in the missing energy correction, which will vary by about 1% of the reconstructed energy; the SD reconstruction on the other hand could vary by as much as 25% due to the different depths of shower maximum predicted by different models. The FDs can thus produce a significant contribution to spectrum measurements.

In this paper, we report the cosmic ray energy spectrum above 10<sup>17.5</sup> eV. In Section 2, we describe the Telescope Array FDs. In Section 3, we discuss the event reconstruction and quality cuts, and event simulation methods. In Section 4, we discuss the Monte Carlo (MC) simulation used to calculate the aperture and exposure of this data sample. In Section 4.1, we introduce a new, machine-learning weather classification method using the FDs. In Section 4.2, we discuss the Data/MC comparison used to check the veracity of the aperture calculation. In Sections 5–6 we display the spectrum results with 10 years of exposure, and discuss the spectral features observed. In Section 7, we combine the new TA FD measurement with the previous HiRes FD spectrum measurement [7] which includes data from a very similar measurement technique and with a similar sample size. We again compare the combined spectrum measurement to models to find features in the spectrum and we compare the result to other published cosmic ray energy flux measurements.

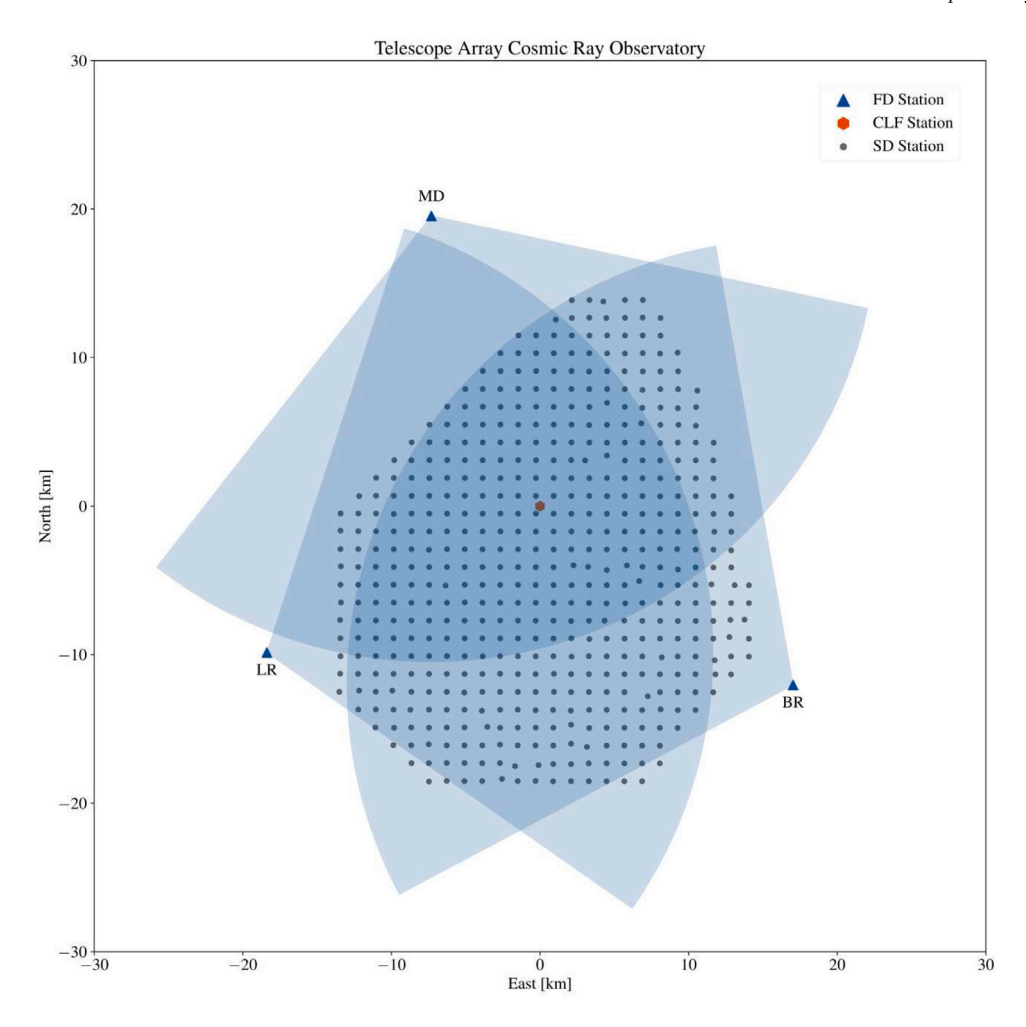


Fig. 1. Map of the Telescope Array Cosmic Ray Observatory. The Fluorescence Detector (FD) stations (blue triangles) are shown with a shaded 30-km field-of-view (FOV) overlooking 507 surface detector stations (dark gray circles), which comprise the surface detector array, and the Central Laser Facility (CLF) (red hexagon).

#### 2. Telescope array cosmic ray observatory

TA is located in Millard County, Utah (see Fig. 1) due to the location's dry, desert air and distance from major light pollution sources. TA has three FD stations composed of a set of fluorescence telescopes viewing from 3° to 33° in elevation and 108° (BR and LR) or 120° (Middle Drum station) in azimuth. The telescopes collect the fluorescence light produced by nitrogen molecules as particles of the cascade, started by the primary cosmic ray, traverse the atmosphere. These FDs remotely sense the cosmic ray Extensive Air Shower (EAS). The telescopes are comprised of a  $16 \times 16$  grid of photomultiplier tubes (PMTs) and a primary mirror. TA's second detection method is an array of 507 surface detectors (SDs) arranged in a square grid with 1.2-km spacing. The SD array detects the footprint of the cosmic ray EAS on the ground.

### 2.1. FADC fluorescence detectors at the telescope array cosmic ray observatory

The BR and LR FD stations [16], and the EAS events they observe, are the focus of this paper. BR and LR are identical stations located on the southeast and southwest, respectively, edges of the surface array. Both stations are comprised of 12 fluorescence telescopes that are arranged in two stacked rows of six to cover  $3^{\circ}$  to  $33^{\circ}$  in elevation and  $108^{\circ}$  in azimuth. Each fluorescence telescope is composed of a segmented, spherical primary mirror which collects fluorescence light from the atmosphere onto a  $16 \times 16$  grid of hexagonal PMTs, the camera, at the focal plane of the telescope. The BR and LR station use

flash analog-to-digital converters (FADCs) for digitization of the PMT signals which feeds into the triggering readout of the FD signals [17]. The photometric calibration of the PMTs at the BR and LR stations was performed before installation by Calibration by RAYleigh Scattering (CRAYS) [18]. The relative photometric gains of the PMTs is monitored over time after installation by a small YAP scintillator (YAlO<sub>3</sub>:Ce scintillator with embedded  $^{241}\mathrm{Am}~\alpha\text{-source}$ ) placed on a few PMTs in each camera [19].

These fluorescence detectors operate on clear, moonless nights. They observe the light profile produced by the excited nitrogen along the EAS track in the atmosphere. Ultimately, these FDs observe the calorimetric energy of the EAS, the energy deposited by the initial cosmic ray in the atmosphere.

#### 3. FD monocular cosmic ray event reconstruction

Events observed by a single FD are reconstructed in the following fashion: the geometry of the EAS core relative to the FD station is determined, then the calorimetric energy of the EAS is determined by reconstructing the charged particle profile along the core. Finally, to account for EAS particle energy not deposited in the atmosphere, an invisible energy correction is applied. The reconstruction methods of fluorescence events are traced back to previous FD experiments, HiRes [20] and Fly's Eye [21]. An independently developed implementation of fluorescence data analysis has also been used by TA [14], and those methods have validated the methods described here.

#### 3.1. Shower detector plane

The first step in geometry reconstruction is the determination of the Shower Detector Plane (SDP), the plane containing the line of the EAS core and the point of the FD station. The SDP is determined by minimizing  $\chi^2$  in the following equation,

$$\chi^2 = \sum_{i=1}^{N_{\text{good}}} (\hat{n} \cdot \hat{v_i})^2 N_{\text{pe},i},\tag{1}$$

to determine the normal vector of the SDP,  $\hat{n}$ , using the pointing direction,  $\hat{v}_i$  of the triggered PMTs weighted by the PMT signal  $N_{\mathrm{pe},i}$ . The PMTs to be included in this minimization are called "good" tubes, to be differentiated from the "noise" tubes which are not part of the event. The collection of good PMTs is determined by a clustering algorithm and iteration [7,14].

#### 3.2. Geometry

The next step is to reconstruct the geometry of the EAS core within the SDP using the timing of the triggered PMTs,  $t_i$ , and the PMT pointing direction in the SDP plane,  $\alpha_i$ , by  $\chi^2$ -minimization using the fit-function

$$t_i = t_0 + \frac{R_p}{c} \tan\left(\frac{\pi - \psi - \alpha_i}{2}\right),\tag{2}$$

with the time offset,  $t_0$ , the impact parameter  $R_p$  and the EAS core inclination angle,  $\psi$  as free parameters. The geometric parameters are illustrated in Fig. 2.

#### 3.3. Energy

Once the geometry is determined, we can account for the atmospheric scattering and absorption of the photon flux that reaches the FDs and produces a signal in the detector. Atmospheric scattering is calculated assuming Rayleigh scattering from the atmosphere using atmospheric profiles calculated from the Global Data Assimilation System (GDAS) database for the position TA every three hours [22]. Atmospheric scattering also includes Mie scattering from aerosols using a vertical aerosol optical depth (VAOD) of 0.04 with scale height of 1 km. The longitudinal light profile, adjusted for these scattering effects, is converted to a charged-particle profile using the experimentally estimated atmospheric fluorescence yield [23] along with the relative fluorescence spectrum as measured by the FLASH collaboration [24,25]. This charged-particle profile,  $N_{\rm ch}(X)$ , is parameterized as a function of slant depth, X, using the Gaisser–Hillas function [26],

$$N_{\rm ch}(X) = N_{\rm max} \left( \frac{X - X_0}{X_{\rm max} - X_0} \right)^{\frac{X_{\rm max} - X_0}{\Lambda}} \exp \left( \frac{X_{\rm max} - X}{\Lambda} \right). \tag{3}$$

The parameters of the Gaisser–Hillas function are:  $N_{\rm max}$ , the number of shower particles at maximum development;  $X_{\rm max}$ , the slant depth of maximum development;  $X_0$ , the approximate start of the shower; and  $\Lambda$ , the decay parameter of the shower. The charged particle profile is used to determine the energy deposited in the atmosphere using the mean ionization energy of the electrons in the EAS [27]. Summing the energy deposited over the entire longitudinal development of the EAS, the energy deposited in the atmosphere by the EAS, gives the calorimetric energy of the primary cosmic ray,

$$E_{\rm cal} = \int_{X_0}^{\infty} \frac{dE_{\rm dep}(X)}{dX} dX. \tag{4}$$

The muons and neutrinos produced in the EAS are more likely to continue away from the EAS and do not interact with the atmosphere. Therefore this energy that is not deposited needs to be accounted for. To account for this, an invisible energy correction function is applied

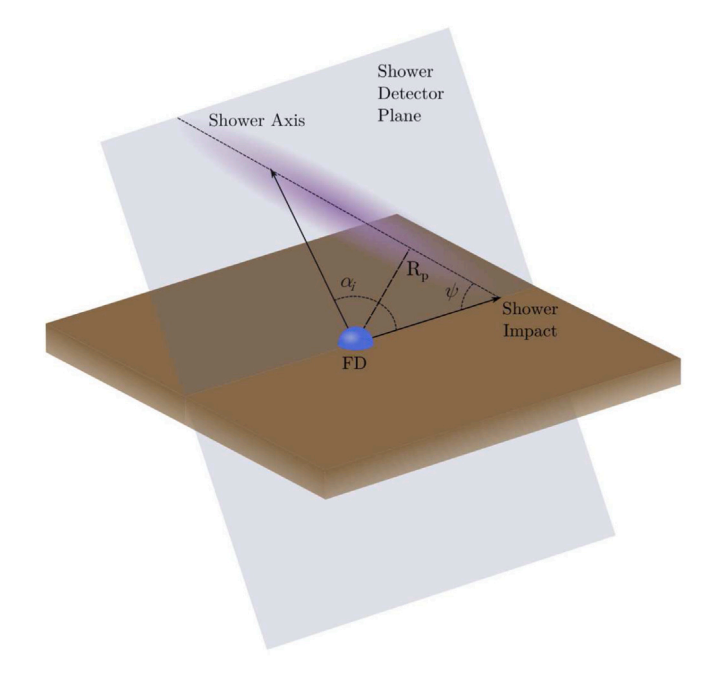


**Fig. 2.** The geometric parameters used in time fitting.  $\psi$  is the angle between the shower axis and the direction from the shower impact to the FD.  $\alpha_i$  is the angle viewed by a PMT in the shower detector plane up from the ground.  $R_P$  is the distance of closest approach of the shower axis to the FD. [32].

to determine the initial energy of the cosmic ray before its interaction with the atmosphere.

$$\frac{E_{\text{cal}}}{E_0} = -0.5717 + 0.1416 \log_{10}(E_{\text{cal}}/\text{eV}) - 0.003328 \log_{10}(E_{\text{cal}}/\text{eV})^2.$$
 (5)

This invisible energy correction is created from simulations of protonic cosmic rays in the atmosphere and tracking the particles such as the muons and neutrinos produced in the EAS using the composition fraction of iron and proton from HiRes-MIA [28] and HiRes [29]. There are methods to estimate the invisible energy directly from data [30] and we have verified the consistency of our invisible energy correction using a similar method [31].

#### 3.4. $R_{X_{max}}$

We introduce a new parameter in this analysis,  $R_{X_{\max}}$ .  $R_{X_{\max}}$  is the distance from the FD station to the position of  $X_{\max}$  along the shower core as shown in Fig. 3.  $R_{X_{\max}}$  is introduced as another distance parameter to understand the FDs sensitivity to the brightest part of the EAS. While  $R_p$ , the impact parameter, from Eq. (2), is the closest distance from the EAS core to the FD station, it does not necessarily correspond to the portion of the shower to which the FDs are sensitive.  $R_{X_{\max}}$  is calculated using the reconstructed  $X_{\max}$  which represents a physical property of the EAS as it describes the maximum development of the shower in Eq. (3).

We calculate  $R_{X_{\mathrm{max}}}$  by determining the height, h, where  $X_{\mathrm{max}}$  occurs,

$$h(X_{\text{max}}, \theta_{\text{zen}}, h_0) = X^{-1}(X_{\text{top}} - X_{\text{max}}\cos(\theta_{\text{zen}})) - h_0,$$
 (6)

where

$$X_{\text{top}} = 1033.22 \text{ g/cm}^2,$$
 (7)

and  $X^{-1}$  is the inverse function of slant depth to height calculated numerically using the density of the atmosphere from the US Standard Atmosphere 1976 [33].  $h_0$  is the height (elevation) at ground level. Then using the reconstructed parameters of the shower axis, we can determine the projection on the ground of  $X_{\rm max}$  relative to the FD

#### Table 1

BR and LR monocular event geometry-reconstruction quality cuts with parameters for events that are kept. In this table,  $N_{\rm Good~PMT}$  refers to the number of PMTs determined to be participating in the event, while  $N_{\rm PMTs}$  refers to all triggered PMTs. The track length  $\Delta\theta$  refers to the angular span of the directions of the PMTs along the SDP. The pseudo-distance is the average angular speed of the event,  $\Delta\theta/\Delta t$  divided by c. The SDP angle is the angle between the SDP and vertical as projected on the camera. The track length cut is applied separately for events which only exist in the lower tier of cameras, "Ring 1", as opposed to those which appear in both tiers or only in the upper tier, "2-Ring" events. Crossing Time refers to when the fit value  $t_0$  occurs within the trigger time-frame and removes accidental triggers.

Event geometry reconstruction cuts.	
Good PMT Fraction	$N_{\rm Good\ PMT}/N_{\rm PMTs} \ge 3.5\%$
Number Good PMTs	$N_{\rm Good\ PMT} \ge 6$
NPE per Degree	$N_{\rm pe}/\Delta\theta > 25$ NPE/deg.
Pseudo-distance (angular speed of EAS)	$r_p > 1.5 \text{ km}$
SDP Angle	≤ 80°
$R_p$	$R_p \ge 0.5 \text{ km}$
$\psi$	$\psi < 130^{\circ}$
$\psi$ fit uncertainty	$\sigma_{\psi} < 36^{\circ}$
	Successful Timing Fit
Timing Fit	$\chi^2$ /n.d.f. < 10
Track Length in Ring 1	$\Delta\theta_{\mathrm{Ring}} \ _{1} > 7^{\circ}$
Track Length 2-Ring	$\Delta\theta_{\rm Ring~2} > 10^{\circ}$
Zenith Angle	$\theta_{\rm zen} < 70^{\circ}$
Crossing Time	$t_0 < 25.6 \ \mu s$
Time Duration	$\Delta t > 6 \mu s \text{ (for } R_p < 5 \text{ km)}$

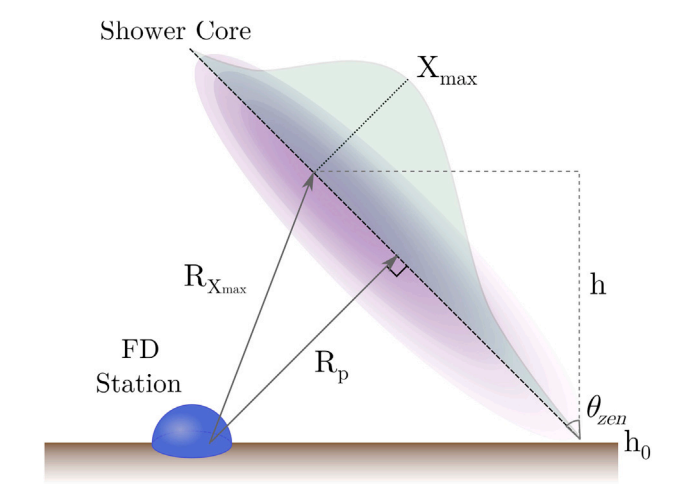


**Fig. 3.** The  $R_{X_{\max}}$  parameter vs shower impact parameter,  $R_p$ , for a fluorescent event with the shower development overlaid on top of the shower core.

station to then ultimately determine  $R_{X_{\max}}$ . The atmospheric model used to calculate  $R_{X_{\max}}$  is different than the GDAS model used in the calculating the attenuation of the fluorescence signal, however, this has only a limited impact on the accuracy of the  $R_{X_{\max}}$  vector, typically of order 10 m on a vector of magnitude 20 km.

#### 3.5. Reconstruction quality cuts

We apply quality cuts to the reconstructed data set to remove poorly reconstructed events and events with hard to reproduce properties. The quality cuts fall into two categories: Geometry (Table 1) and Profile (Table 2). These quality cuts are applied to the Monte-Carlo-simulated cosmic-ray events used in the later stages of this analysis as well.

#### 4. Aperture and exposure calculations

We use Monte Carlo (MC) simulations to determine the detection aperture of the FDs. The details of this calculation are identical to the MC calculation presented in Ref. [13]; we reiterate some of the details here. MC events are produced by choosing random event geometries

#### Table 2

BR and LR monocular event profile reconstruction quality cuts with parameters for events that are kept. All depths are slant-depths in the atmosphere which are determined from the pointing directions of the PMTs combined with the geometry of the shower axis determined in the time fitting.

Event profile reconstruction cuts	
	Successful Profile Fit
First Depth Observed	$150 \text{ g/cm}^2 \le X_1 \le 1200 \text{ g/cm}^2$
Observed Depth Extent	$\Delta X \ge 150 \text{ g/cm}^2$
$X_{\rm max}$ Bracketing	$X_{\rm max}$ is contained within the field-of-view

and EAS parameters, throwing them over a simulated array, simulating fluorescence light production along the EAS, accounting for light propagation and atmospheric effects between production and the detectors, and finally simulating the response of the detectors to the light from EAS. The EAS parameters are chosen at random from a library of CORSIKA [34]-generated UHECR longitudinal profiles. This process of generating events allows us to determine the detection aperture given the number of accepted events divided by the number of thrown events within a defined simulation volume. We define the MC-simulation volume as a ground area of a 1° spherical polar cap around the central laser facility (CLF) (a circle of radius of ~ 111 km) with arrival directions of all azimuthal angles and zenith angles up to 80°. This comes to a geometric aperture  $A_0 \Omega_0 = 1.18348 \times 10^{11} \text{ m}^2 \text{ sr. We produced}$ a number of reconstructed MC events roughly five times the number of observed events to make the statistical effects of the MC sample negligible. We selected MC event energies between 10<sup>16.5</sup> and 10<sup>21.5</sup> eV according to the previously observed spectrum presented by TA at the ICRC 2015 [35] and composition according to that measured by HiRes-Mia [28] and HiRes [29]. By simulating the flux according to a previously measured spectrum, our MC minimizes the systematic effect of bin-to-bin migration of events due to reconstruction. Remaining binto-bin migration effects are accounted for in the acceptance calculation where the numerator is binned by reconstructed energy while the denominator is binned by thrown energy [7,13,14]. For each event the response of both BR and LR FD stations is simulated to account for the overlap of the field-of-view of the two stations. This simulation of both detectors for all events allows an estimation of the separate monocular exposures of BR and LR and the tandem-stereo exposure for events that trigger both detectors. The process of combining the three components will result in a combined exposure (and later to a combined spectrum).

The monocular-combined exposure using the aperture,  $A\Omega$ , and live-time, T, of BR, LR, and the tandem-stereo intersection is calculated as

$$\xi(E)_{\mathrm{BR}\cup\mathrm{LR}} = A\Omega(E_i)_{\mathrm{BR}}\,T_{\mathrm{BR}} + A\Omega(E_i)_{\mathrm{LR}}\,T_{\mathrm{LR}} - A\Omega(E_i)_{\mathrm{BR}\cap\mathrm{LR}}\,T_{\mathrm{BR}\cap\mathrm{LR}}. \tag{8}$$

The intersecting region (BR $\cap$ LR) of tandem-stereo events is removed so as to not double count events. The exposures, shown in Fig. 4, were fit to smooth out statistical fluctuations at higher energies using the function,

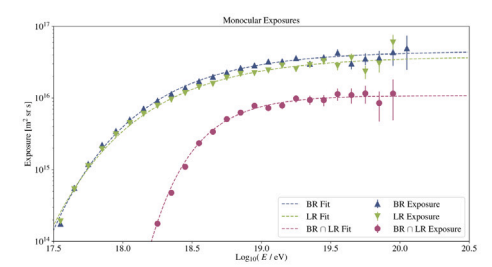
$$\log_{10} \xi(E) = p_1 \left( 1 - \exp\left[ -\frac{\log_{10}(E/\text{eV}) - p_2}{p_3} \right] \right). \tag{9}$$

For fits to the BR, LR and the monocular-combined apertures, the lower energy bound in the fit is  $\log_{10}(E/\text{eV}) = 17.6$ , while for the tandemstereo aperture, the lower energy bound is  $\log_{10}(E/\text{eV}) = 18.5$ . The exposure fit results are listed in Table 3.

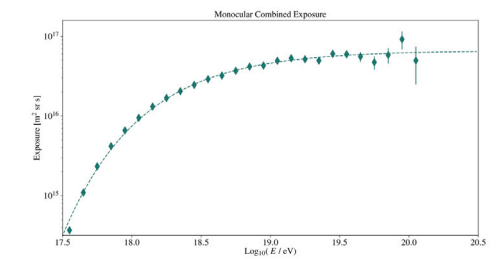
At energies below the bounds of the fits, the bin-by-bin calculation of the exposure is used with interpolation from the center of the bins. The MC has a much greater number of events at these lower energies which allows for an exposure calculation with small statistical fluctuations. The full exposures are shown in Fig. 5.

#### 4.1. Machine learning weather classification

A new weather classification method was introduced with this analysis to determine which FD data parts had good weather and thus



(a) BR, LR, and tandem-stereo exposures vs. reconstructed energy.



(b) Monocular-combined exposure vs. reconstructed energy.

Fig. 4. Monocular exposure fits.

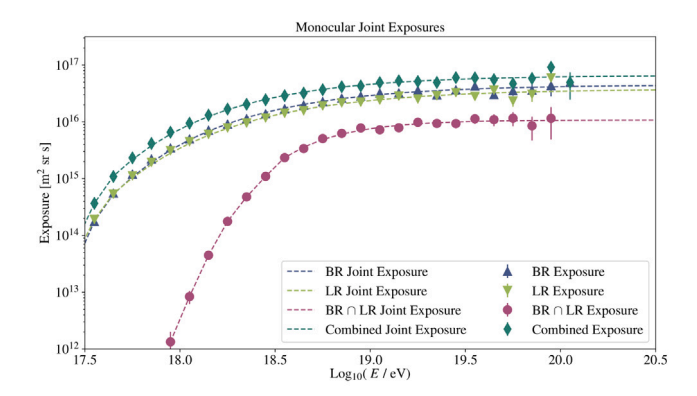


**Fig. 5.** BR, LR, stereo, and the monocular-combined exposures. The exposure combines the calculated exposure at low energies with the fit exposure given by parameters listed in Table 3.

will be used in this analysis. An FD data part refers to a contiguous period of data collection by one of the FDs with trigger parameters set to gather data from EASs. These data collection periods are interspersed with calibration data collection periods. The FD data parts collect a predetermined number of triggers in the range 3,000–12,000. The FD data parts have a typical duration of up to an hour. An FD data part is the finest level at which we can select data based on good or bad weather conditions.

In bad weather, when there are clouds within the field-of-view, the light profile or light track can be distorted, resulting in poor geometry and energy reconstruction of events. In previous TA analyses weather classification relied on hourly visual observations of the night sky taken by the operators at the Middle Drum (MD) FD station. These observations are somewhat subjective and rely on the weather at MD being not too different from that at the BR and LR stations 30 km away.

We designed a new, objective method using machine learning that can be performed independently at both the BR and LR stations. We built upon a method used for BR and LR data to take the minute-average pedestal of each PMTs FADC traces and using the nominal pointing direction of the PMT to create a false-color image of the night sky every minute. This method relies on the DC-coupled PMT arrangement at BR and LR. Since there is a PMT pedestal value for each minute of operation of both BR and LR FD stations, we created an animation of the field-of-view (FOV) for each FD data part. To enhance the features of these animations, we took the frame-to-frame differences to highlight moving objects and then logarithmically normalized these differenced frames. Within these animations, one can see stars move across the FOV in clear weather, and the edges of clouds move across the FOV in cloudy weather.

To classify each FD data part for both BR and LR, a recurrent convolution neural network (RCNN) was designed and trained to classify each FD data part as either clear, cloudy, or noisy. A noisy FD data

**Table 3**Monocular exposure fit parameters.

	$p_1$	$p_2$	$p_3$	$\chi^2$ /ndf
BR	$16.65 \pm 0.03$	$16.40 \pm 0.09$	$0.58 \pm 0.04$	10.64/23
LR	$16.58 \pm 0.03$	$16.31 \pm 0.10$	$0.61 \pm 0.04$	13.64/22
$BR \cap LR$	$16.03 \pm 0.05$	$17.57 \pm 0.28$	$0.32 \pm 0.29$	3.91/12
$BR \cup LR$	$16.82 \pm 0.02$	$16.39 \pm 0.09$	$0.56 \pm 0.03$	9.83/23

**Table 4** RCNN structure. The input layer is  $t_{\rm max}$  frames from the 2 × 6 cameras each with  $16 \times 16$  pixels. The time-distributed convolution layers do convolutions on each frame separately.

Input layer	$96 \times 32 \times t_{\text{max}}$ pixels
1st time-distributed convolution layer	$8.4 \times 4$ conv. filters
2nd time-distributed convolution layer	$8.4 \times 4$ conv. filters
1st long short term memory (LSTM) layer	48 nodes
2nd LSTM layer	6 nodes
Output layer	3 nodes

part was a data part where the animation showed noisy pixels and nothing could be distinguished within the FOV. Noisy data parts can be caused by lightning or an external light source overloading the detector electronics or a period where the detectors were not operating properly.

An RCNN was chosen as the recurrent layers train on the temporal information and the convolution layers train on the spatial information. The structure of the RCNN is given in Table 4. It consists of two time-distributed convolution layers, followed by two long short-term memory (LSTM) layers [36], finally resulting in three output nodes. The convolution layers identify stars (points) and cloud edges (lines). The LSTM layers track the features found in the convolution layer through the time sequence. The three outputs are clear, cloudy, and noisy.

To train the RCNN, 20% of BR and LR animations were selected, uniformly randomly sampled in time. These animations were classified by eye as clear, cloudy or noisy. In order to feed all the animations for training as three-dimensional arrays, each array was zero-padded with empty frames. This resulted in each animation being  $t_{\rm max}$  frames long. There are separate  $t_{\rm max}$  values for BR and for LR sites because of differences in running conditions. The RCNN was trained with two-thirds of these samples, and then validated with the remaining third. The training and validation were done separately for the two sites. There will be differences in the BR RCNN and the LR RCNN because the motion of stars will be rising in the LR animations, while falling in the BR animations. We achieved greater than 90% accuracy with this RCNN for both BR and LR. The training information with the RCNN for BR and LR is displayed in Table 5. The confusion matrix resulting from the validation stage at both BR and LR is shown in Table 6.

We then classified all of the FD data parts for BR and LR with their trained RCNN. We mapped the weather classification of the FD data part to all events contained within that data part. The results of this weather classification on all FD data parts and events for BR and LR are displayed in Table 7. Detailed plots of accuracy and loss plots vs. training epoch may be found in [32].

Table 5
BR and LR RCNN weather classification results.

Station	t <sub>max</sub>	Training epochs	Optimizer	Computation time	Validation accuracy	Validation cross entropy
BR	216	50	Adagrad	2:16:11 h	90.93%	0.29
LR	131	50	Adagrad	0:36:57 h	94.31%	0.19

Table 6
BR and LR RCNN classification confusion matrices from the validation stage. In both matrices, the RCNN classification is on the columns while the "true" classification (by-eye) is on the rows. It is worth noting that the true noisy classification is less than 0.1% of all animations.

BR	Clear	Cloudy	Noisy
Clear	0.90	0.10	0.00
Cloudy	0.06	0.94	0.01
Noisy	0.13	0.27	0.60
LR	Clear	Cloudy	Noisy
Clear	0.95	0.05	0.00
Cloudy	0.07	0.93	0.00
Noisy	0.25	0.75	0.00

Table 7

BR and LR weather classes for each FD data part and mapped to each reconstructed event. "Missing" refers to data parts where the RCNN could not be run due to very short extent or missing calibration information.

BR	Clear	Cloudy	Noisy	Missing
FD Data Parts	11,199	7,113	141	243
rb bata raits	(59.9%)	(38.0%)	(0.8%)	(1.3%)
FD Events	15,636	9,346	24	10
rD Events	(62.5%)	(37.4%)	(0.0%)	(0.1%)
LR	Clear	Cloudy	Noisy	Missing
	Clear 10,753	Cloudy 4,750	Noisy 22	Missing 201
LR FD Data Parts				
	10,753	4,750	22	201

From this weather classification method 70% of BR data parts and 60% of LR data parts were clear and could be used for further analysis. Only the events contained within the clear data parts contributed to the event distribution used for the spectrum calculation, and the duration of the clear data parts, accounting also for electronics dead-time, was used as the live-time in the exposure calculation.

The level of consistency of the new RCNN weather classification with the older method is shown in the correlation matrices given in Table 8 for BR/LR data parts which directly overlap with MD weather observations. The old method consists of observations made by the MD operators, a visual inspection of the clarity of the atmosphere. This observation is stored as a code which tells absence or presence of clouds in different parts of the sky. A 0 or 1 is given for the low part of the sky (from the horizon up to 30°) in each of the four quarters; 0 being clear, 1 being cloudy. For the portion of the sky overhead (within 60° of zenith), a score of 0-4 is given, with 0 being completely clear, 1 being up to a quarter covered by clouds, 2 being up to half covered, 3 being up to three quarters covered, and 4 being completely covered (above three quarters). Previous analyses have condensed these codes into "Excellent" weather where all five values are 0, i.e., completely clear, and "Good" weather, where the sum of all the scores is 2 or less, e.g., clouds in one quarter and < 25% coverage overhead. Observations are made at least once every hour, and these observations are then correlated with the BR and LR data parts. The BR and LR data parts are then classified as "Excellent" and "Good" ("Good" parts include all the "Excellent" parts). The set of parts complementary to "Excellent" and to "Good" we will call "Not Excellent" and "Not Good". We can thus form a correlation matrix of the RCNN weather classification against the operator observation categories. These correlations are displayed in Table 8. We can thus see that the RCNN weather classification of

Table 8

Correlation matrix for the output of the RCNN weather determination vs. the MD weather Excellent and Good. Only BR/LR data parts which overlap with a weather observation are included.

BR	Excellent	Not Excellent	Good	Not Good
Clear	3874	2317	5165	1026
Cloudy	307	3211	649	2869
Noisy	0	4	1	3
LR	Excellent	Not Excellent	Good	Not Good
Clear	3406	2477	4615	1268
Cloudy	79	2087	232	1934
Noisy	1	4	1	4

"Cloudy" only corresponds to "Excellent" weather in the BR data in 307 out of 4181 data parts, or 7.3% of cases. The correlations listed in Table 8 are not a confusion matrix for the RCNN model and do not indicate the quality of the model. Rather the correlations show how the previous method of selecting good weather worked reasonably well, and also how it fell short. The correlations indicate that we may have been including about 10% of data that was actually bad-weather data, but not including 20%–40% of data that was actually good-weather data.

As the rates of misidentification may vary with the typical weather, the rate of misidentifying "Excellent" weather with the RCNN "Cloudy" determination given by month of the year is shown in Fig. 6.

We have found a 10% difference in clear FD data parts between BR and LR. The previous method had assumed they were the same. This is now shown not to be the case.

The new weather classification method is objective compared to the previous method, can be performed independently for BR and LR, and allows better timing resolution for the weather progression through the night.

#### 4.2. Data/MC comparisons

To verify the aperture calculation, we show that the geometry distribution of the reconstructed MC and the observed events match each other well. To do this, we show Data/MC comparison plots of the binned, reconstructed MC events (renormalized to the size of the data, for direct comparison) and observed events for the BR and LR for the new parameter  $R_{X_{\rm max}}$ ,  $\psi$ , and  $\theta_{\rm SDP}$ . Evidence of a good Data/MC comparison, is that the MC and observed event distributions should match each other well. As further evidence of good comparisons, we show the Data/MC ratio for each bin of the observed and MC (hence Data/MC) and fit with a polynomial. Good Data/MC agreement in the ratio will have a linear fit with a slope of zero within uncertainty.

The Data/MC comparison for  $R_{X_{\rm max}}$  is shown in Fig. 7, demonstrating that the MC is placing events at appropriate distances from the detector. This comparison using  $R_{X_{\rm max}}$  gives more confidence in the accuracy of the response of the MC simulation of the location of showers than would the similar comparison of  $R_P$ . The Data/MC comparison for  $\psi$  is shown in Fig. 8, and for  $\theta_{\rm SDP}$  in Fig. 9, both showing that the MC represents the appropriate angular distributions of observed events. We do see a curvature in the Data/MC ratio for  $\theta_{\rm SDP}$ . This is the result of the pointing resolution of the telescopes not being modeled precisely in the MC. We have treated this discrepancy as an added systematic uncertainty in the aperture calculation. The maximum of the Data/MC ratio parabolic fit is  $1.11 \pm 0.05$  for BR and  $1.12 \pm 0.04$  for LR. This is in the center of the distribution for vertical SDPs. There is a corresponding deficit of a similar size towards tipped SDPs. We therefore take an 11% systematic error on the flux due to this uncertainty.

In addition to showing the agreement between data distributions and MC generated distributions, we show in Fig. 10 that the energy reconstruction has a resolution of 10%-11% (from the fit width) with a bias (from the distribution means) of less than a 1%, except for the highest energy range where the bias may be as big as 2.6%.

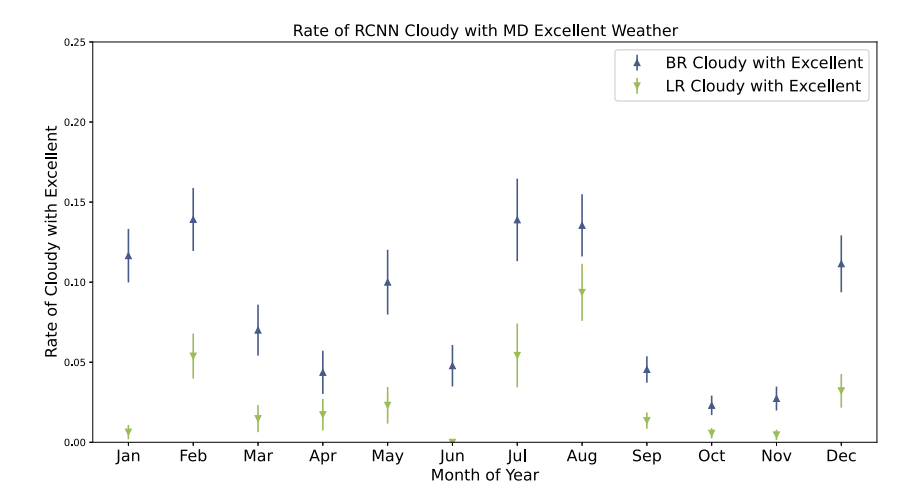


Fig. 6. BR and LR rates of Cloudy weather determination when the MD determination was Excellent weather, broken down by month-of-the-year.

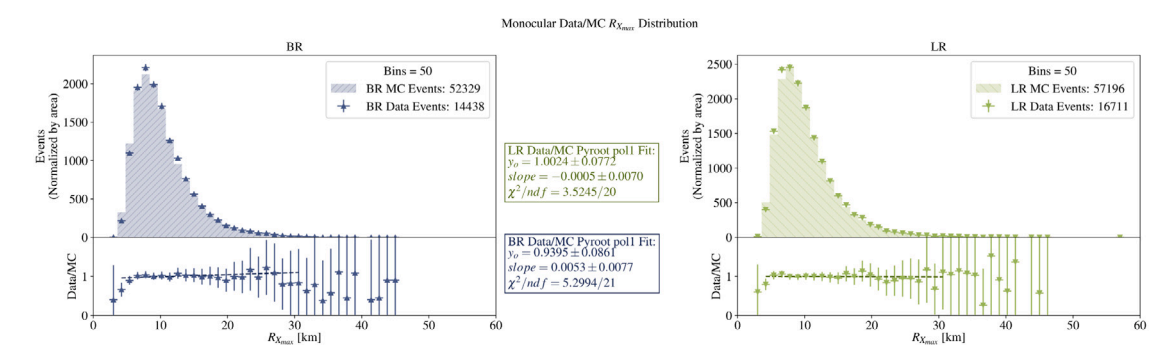


Fig. 7. BR and LR  $R_{X_{\rm max}}$  Data/MC comparison.

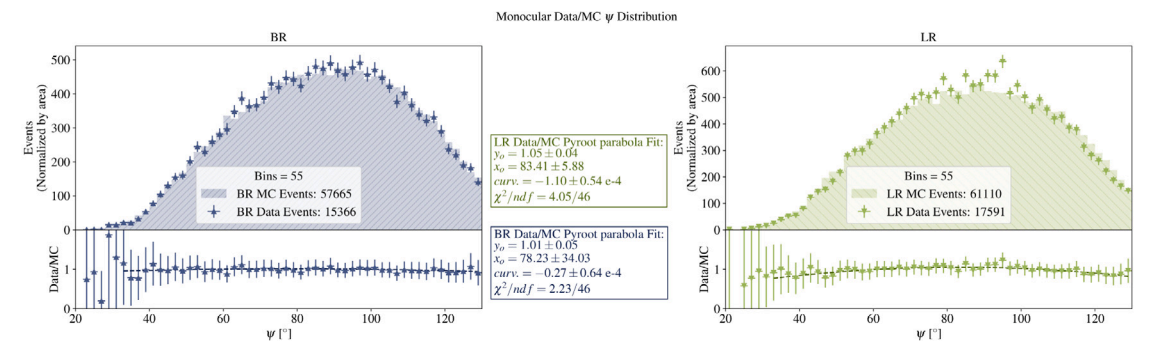


Fig. 8. BR and LR  $\psi$  Data/MC comparison.

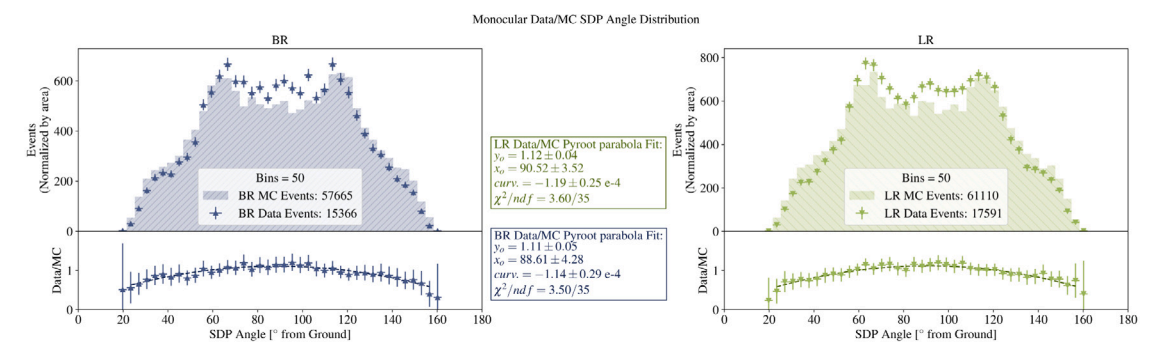


Fig. 9. BR and LR SDP Angle Data/MC comparison.

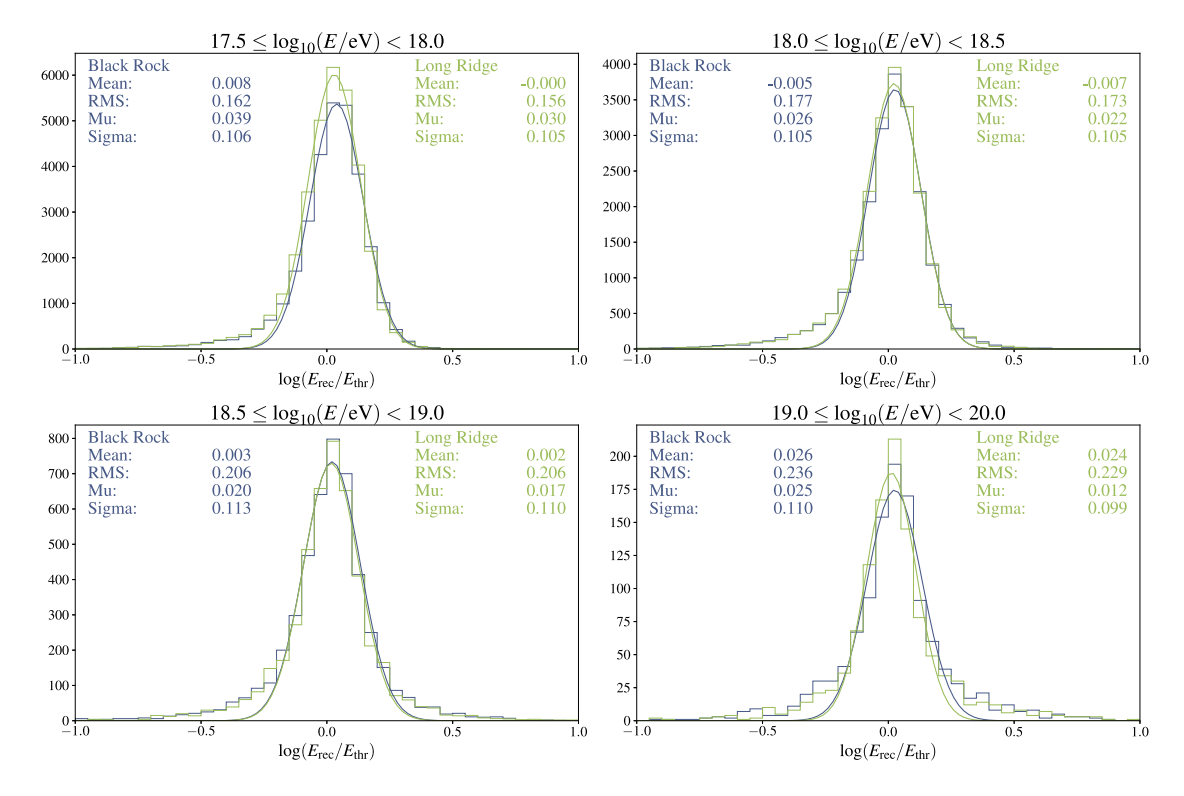


Fig. 10. BR and LR energy resolution obtained in the MC calculation. A histogram of the logarithm of the ratio of reconstructed to thrown energies is shown for each site in four energy ranges. The histograms are fit to normal distributions over the whole range of ratios shown. The mean and the RMS of each histogram is displayed for each site, as well as the mean (Mu) and width (Sigma) of the fit normal distributions. The logarithm of the ratio is chosen so that the RMS and width values can be easily interpreted as percentages.

#### 5. Monocular BR and LR combined energy spectrum

The observed events for both the BR and LR FD stations in monocular mode are combined to increase the statistics for a spectrum calculation. These events were collected with BR and LR station 2008/04/01–2017/11/28, just under 10 years. To account for the region of overlap in events observed by both stations, the event distributions for BR, LR, and events observed by both stations, stereo, were combined as

$$N(E_i)_{BR \cup LR} = N(E_i)_{BR} + N(E_i)_{LR} - N(E_i)_{BR \cap LR}$$
(10)

so as to not double-count events. Tandem stereo events were counted as events seen by both BR and LR stations with a 100- $\mu s$  time-matching window. The tandem stereo event energy was determined by taking the geometric mean of the two station observations of the event,

$$E_{\text{Stereo}} = E_{\text{BR} \, \cap \, \text{LR}} = \sqrt{E_{\text{BR}} \times E_{\text{LR}}}. \tag{11}$$

The TA monocular individual, stereo, and combined event distributions are displayed in Fig. 11.

With the combined event distribution,  $N(E_i)_{\text{Combined}}$ , the bin size,  $\Delta E_i$ , and combined exposure,  $\xi(E_i)_{\text{Combined}}$ , the monocular combined spectrum is calculated as

$$J(E_i)_{\text{BR}\cup\text{LR}} = \frac{N(E_i)_{\text{BR}\cup\text{LR}}}{\Delta E_i \, \xi(E_i)_{\text{BR}\cup\text{LR}}} \tag{12}$$

The separate monocular spectra (multiplied by  $E^3$  to enhance the spectral features) for BR, LR, and stereo, are shown in Fig. 12. The ankle feature is apparent in all three spectra. The LR spectrum is offset above the BR spectrum, but the spectra are parallel as a function of energy, agreeing on the position of the ankle feature and on the spectral slopes from  $\log_{10}(E/\text{eV})=17.5$  to  $\log_{10}(E/\text{eV})=19.3$  above which the statistics are low. Although BR and LR are identical stations, there are environmental factors that are different between the stations. The weather classification using machine learning showed a 10% difference in the number of clear weather data parts. BR and LR are separated

by 35 km, and LR is 150 m higher in altitude. As seen with weather classification, the assumption that conditions at the two stations are identical may not hold. Given that the spectra are parallel to each other, it is suggestive that factors in the exposure could be investigated and improved. However, the monocular combined spectrum, by its construction, averages the BR and LR event distributions and exposures, giving a better representation of the true spectrum than the individual spectra.

By combining the measurements of both stations, the event statistics will improve, especially at the higher energies where events are rare. The monocular combined spectrum was calculated using Eq. (12) and is shown in Fig. 13. The monocular combined spectrum compares well with the other individual spectra as they visually follow the same form and match breakpoints. The BR and LR spectra can be brought into an agreement by shifting BR up 5% and LR down 5%, thus we estimate the monocular combined spectra has a 5% systematic uncertainty from the BR and LR offset.

The primary source of systematic uncertainty in the flux calculation comes from uncertainty in the energy scale. Details of the sources of systematic uncertainties in this measurement are the same as in Ref. [13], but we will repeat the dominant sources of uncertainty here. High-energy interaction models were used to calculate the specific fluorescence yield and the invisible energy correction on an event by event basis, resulting in a 11% modeling uncertainty on energy scale. The absolute photometric calibration of the PMTs provides an additional 11% uncertainty. The modeling of light attenuation by aerosols in the atmosphere provides a 10% uncertainty in energy scale. The total energy scale uncertainty from all sources added in quadrature is 21%. Given the power-law nature of the spectrum, the energy scale uncertainty contributes 35% uncertainty in the flux. To this uncertainty we add, in quadrature, the 10% uncertainty in aperture from the SDP angle measurement, and the 5% uncertainty from disagreement between BR and LR separate flux measurements mentioned above. The total systematic uncertainty by combining uncertainties in quadrature is 37% for the monocular combined spectrum (see Table 9).

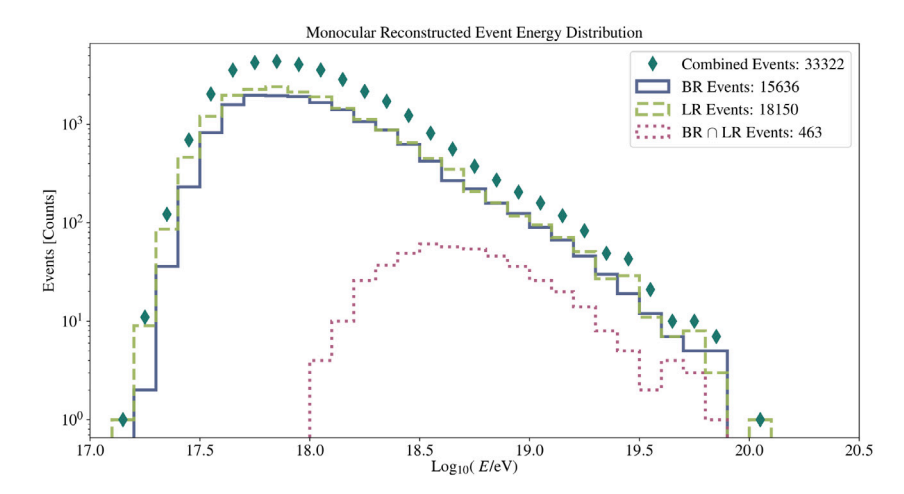


Fig. 11. BR, LR, Stereo, and Combined event distributions.

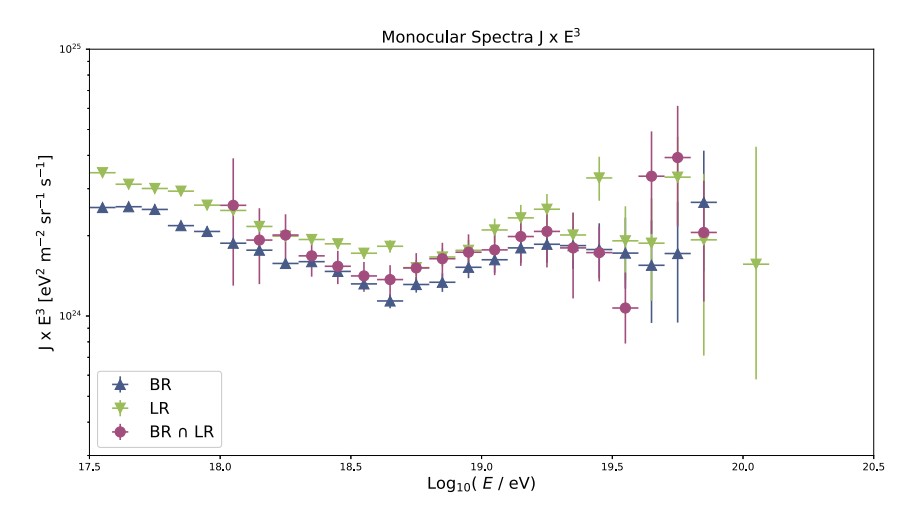


Fig. 12. BR, LR, and BRULR  $J \times E^3$ .

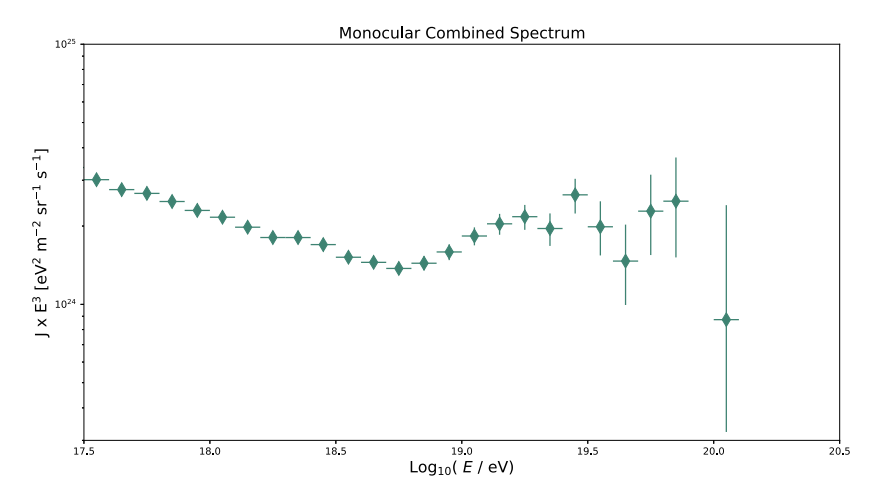


Fig. 13. The monocular combined  $J(E) \times E^3$ .

The monocular combined spectrum measurement compares well with other previous spectrum measurements. The monocular combined spectrum measurement agrees within statistical uncertainty with the TA combined ICRC 2019 spectrum, which used the TA SD array and the TALE fluorescence detectors. The monocular combined spectrum result

also agrees within the statistical uncertainty with the HiRes Experiment monocular FD spectra. These spectra match well with form and breaks (see Fig. 14).

**Table 9** Mono combined spectrum measurements by each bin for bin centers with  $\log_{10}(E/\text{eV}) \ge 17.5$ . Each bin has a size of 0.1 in  $\log_{10}(E/\text{eV})$ . The event counts for the BR, LR, stereo, and the mono combined are listed. The measured spectrum, J(E), is listed with the lower and upper 68% confidence range limits with units of  $[\text{eV}^{-1} \text{ m}^{-2} \text{ sr}^{-1}]$ .

Bin Center	$N_{ m BR}$	$N_{ m LR}$	$N_{\rm BR\cap LR}$	$N_{\rm BR\cup LR}$	$\xi(E)_{\mathrm{BR}\cup\mathrm{LR}}$	$J(E)_{\mathrm{BR}\cup\mathrm{LR}}$	$\sigma_{ m J\ lower}^{ m stat}$	$\sigma_{ m J}^{ m stat}$
17.55	825	1208	0	2033	3.68e+14	6.75e-29	1.50e-30	1.50e-30
17.65	1585	1969	0	3554	1.11e+15	3.10e-29	5.20e-31	5.20e-31
17.75	1969	2269	0	4238	2.17e+15	1.50e-29	2.31e-31	2.31e-31
17.85	1949	2408	0	4357	3.81e+15	7.00e-30	1.06e-31	1.06e-31
17.95	1922	2135	0	4057	6.08e+15	3.24e-30	5.09e-32	5.09e-32
18.05	1665	1904	4	3565	8.99e+15	1.53e-30	2.56e-32	2.56e-32
18.15	1407	1459	10	2856	1.25e+16	7.02e-31	1.31e-32	1.31e-32
18.25	1065	1123	26	2162	1.64e+16	3.21e-31	6.91e-33	6.91e-33
18.35	876	875	37	1714	2.06e+16	1.61e-31	3.89e-33	3.89e-33
18.45	627	652	49	1230	2.49e+16	7.58e-32	2.16e-33	2.16e-33
18.55	424	451	61	814	2.93e+16	3.40e-32	1.19e-33	1.19e-33
18.65	268	350	57	561	3.34e+16	1.63e-32	6.87e-34	6.87e-34
18.75	221	208	54	375	3.74e+16	7.73e-33	3.99e-34	3.99e-34
18.85	158	160	46	272	4.10e+16	4.06e-33	2.46e-34	2.46e-34
18.95	124	117	36	205	4.44e+16	2.25e-33	1.57e-34	1.57e-34
19.05	90	95	26	159	4.74e+16	1.30e-33	1.03e-34	1.03e-34
19.15	67	71	20	118	5.00e+16	7.24e-34	6.66e-35	6.66e-35
19.25	46	51	14	83	5.23e+16	3.86e-34	4.24e-35	4.24e-35
19.35	30	27	8	49	5.44e+16	1.74e-34	2.49e-35	2.49e-35
19.45	19	29	5	43	5.61e+16	1.18e-34	1.80e-35	1.80e-35
19.55	12	11	2	21	5.77e+16	4.45e-35	9.97e-36	1.12e-35
19.65	7	7	4	10	5.89e+16	1.65e-35	5.30e-36	6.27e-36
19.75	5	8	3	10	6.01e+16	1.28e-35	4.13e-36	4.89e-36
19.85	5	3	1	7	6.10e+16	7.02e-36	2.75e-36	3.32e-36
19.95	0	0	0	0	6.18e+16	0.00e+00	0.00e+00	1.02e-36
20.05	0	1	0	1	6.25e+16	6.18e-37	3.90e-37	1.09e-36
20.15	0	0	0	0	6.30e+16	0.00e+00	0.00e+00	6.28e-37
20.25	0	0	0	0	6.35e+16	0.00e+00	0.00e+00	4.95e-37
20.35	0	0	0	0	6.39e+16	0.00e+00	0.00e+00	3.91e-37
20.45	0	0	0	0	6.43e+16	0.00e+00	0.00e+00	3.09e-37

## 6. Spectral features and observation of the high-energy suppression with the monocular BR and LR combined spectrum

#### 6.1. Spectral features above $\log_{10}(E/eV) \ge 17.5$

The cosmic ray spectrum has been observed to roughly follow a broken power law. Different populations of cosmic rays, acceleration mechanisms in the universe, and propagation effects create features in the cosmic ray energy spectrum. These features are brought out by fitting the spectrum with broken power law functions. We fit the spectrum with a series of once, twice, and thrice broken power laws where A is a normalization constant,  $E_i$  represents the location of breakpoints in  $\log_{10}(E/\text{eV})$ , and  $\gamma_i$  represents the spectral indices. Since the spectrum is calculated using observed events, it is proper to minimize the broken power-law fit with Poisson fit deviance,  $D_{\text{Poisson}}$  [37,38], rather than  $\chi^2$ . The Poisson deviance is also sometimes referred to as the Cash statistic [39]. By minimizing the Poisson deviance, we are maximizing the event binned likelihood. Above  $\log_{10}(E/\text{eV}) = 17.5$ , the most prominent break feature is the ankle, thus  $E_1$  represents  $E_{\text{Ankle}}$ . The twice- and thrice-broken fits bring out the spectral features above the ankle.

The results of the series of broken power law fits are shown in Fig. 15 and the fit parameters are listed in Tables 10–12 with the position of the breaks, the spectral indices, and the fit statistics. Two twice-broken fits with comparable fit deviance were found with a lower and higher second break energy. Scanning the position of the second break in the twice-broken fit reveals two minima in the fit deviance of relatively significant values. All of the broken power law fits have an agreement within the uncertainty for the ankle position, except for the once-broken fit. The lower  $E_2$  twice-broken fit is positioned between the  $E_2$  and  $E_3$  positions of the thrice-broken fit, possibly because the twice-broken fit was picking up on the presence of both breaks. The higher  $E_2$  twice-broken fit lines up with the thrice-broken fit so that the fits overlap beyond  $E_3$  in the thrice-broken fit. The

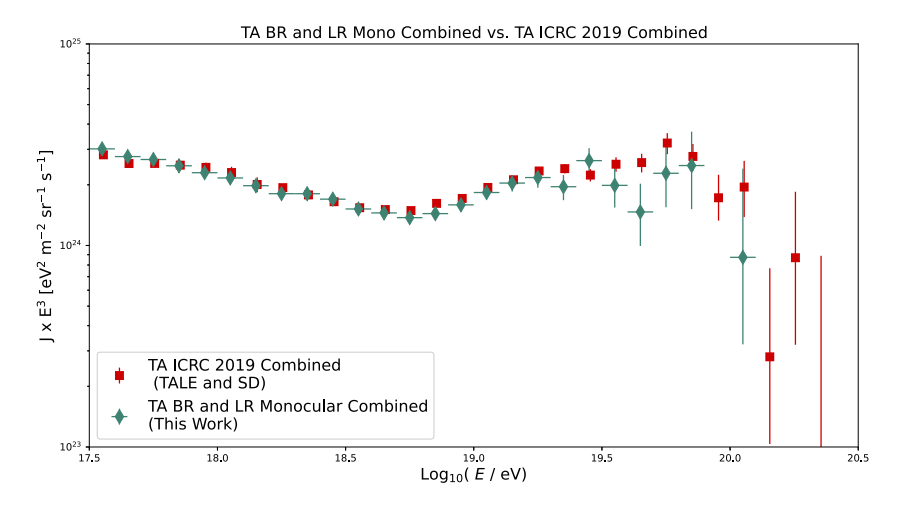
**Table 10** Monocular combined spectrum once-broken power law fit above  $\log_{10}(E/eV) = 17.5$ .

	$J(E)_{ m Once\ Broken}$
$J(E = 10^{18} \text{ eV}) \times 10^{-30} \text{ eV}^{-1} \text{ m}^{-2} \text{ sr}^{-1} \text{ s}^{-1}$	$2.22 \pm 0.01$
$\gamma_1$	$-3.29 \pm 0.01$
$\log_{10}(E_1/\text{eV})$	$18.68 \pm 0.04$
$\gamma_2$	$-2.79 \pm 0.05$
D <sub>Poisson</sub> /ndf	43.45/26

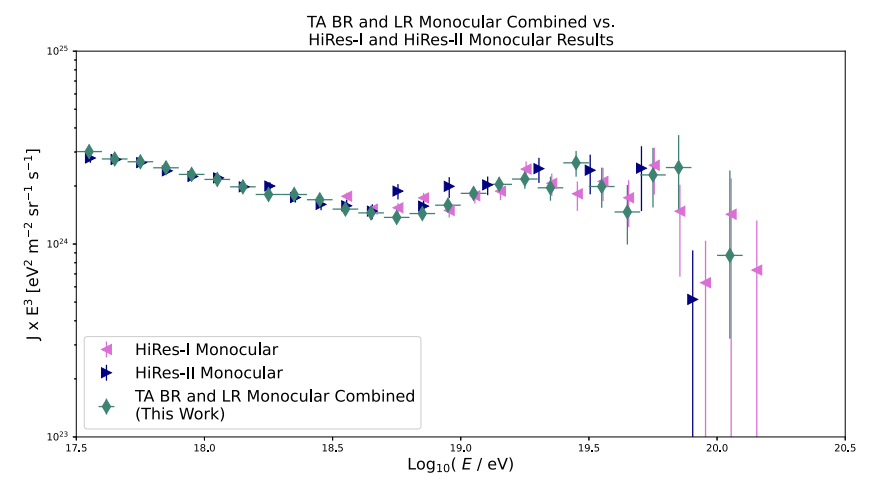
higher  $E_2$  twice-broken fit is in agreement with the previous results of TA SD ICRC 2019 and the HiRes results. Adding each break in the fit lowers the deviance compared to the number of degrees-of-freedom (ndf) significantly. The thrice-broken fit compared to both twice-broken fits reduces the number of degrees-of-freedom by 2 while the deviance drops by five. Since the drop in deviance is greater than the drop in ndf, the thrice-broken power fit is significantly better. Thus, the monocular combined spectrum suggests two breaks beyond the ankle. The last break in the thrice-broken fit can still be attributed to the high-energy suppression, specifically the GZK suppression as observed previously by HiRes and TA.

#### 6.2. Observation of the high-energy suppression

We evaluate the significance of the high-energy suppression of cosmic rays using the monocular combined spectrum. This significance is determined by assuming that the spectral index after the ankle,  $\gamma_2$ , does not break at  $E_2$  in the twice-broken power fit. The higher second break twice-broken fits with the assumed continuation past the second break are shown in Fig. 16. The number-of-events expected is calculated assuming the spectrum continues unbroken beyond  $E_2$  with the measured exposure for each energy bin beyond  $E_2$  to  $E \to \infty$ . We determine the statistical significance of the observed number of



(a) Monocular combined spectrum vs. TA combined ICRC 2019[15] spectrum. The TA combined ICRC 2019 spectrum is offset slightly on the x-axis for ease-of-viewing.



(b) Monocular combined spectrum vs. the HiRes-I and -II[37] monocular spectra. The HiRes-I and -II spectra are offset slightly on the x-axis for ease-of-viewing.

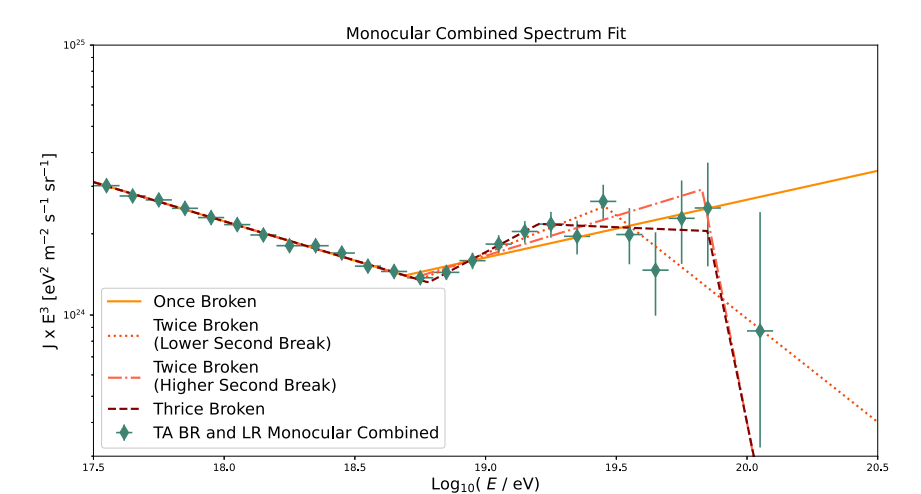


**Fig. 14.** Monocular combined  $J(E) \times E^3$  vs. previous measurements.

Fig. 15. Monocular combined spectrum with once, twice and thrice broken power-law fits above  $\log_{10}(E/eV) = 17.5$ .

events by comparing to the expected number of events of the unbroken flux using the cumulative Poisson probability of observed events vs. expected events. This method evaluates the chance probability of the high-energy suppression which is interpreted as a Gaussian significance in  $\sigma$ . In the higher second break twice-broken fit, which is consistent with previous spectrum results from the northern hemisphere, we expect 26.15 events if the spectrum remains unbroken given the exposure and only 8 event were observed. This has a chance probability of

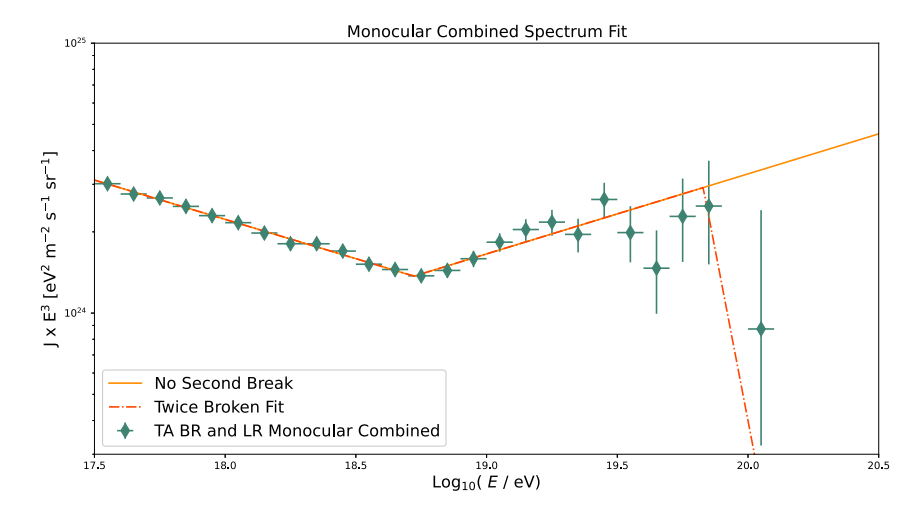


**Fig. 16.** Twice-broken power law fit to the monocular combined spectrum. The solid orange line shows the continuation of the spectral index,  $\gamma_2$ , past the second break  $E_2$  used to calculated the expect number of events if the spectrum remains unbroken above the ankle. The red dashed line shows the full twice-broken power law fit.

Table 11 Monocular combined spectrum twice-broken power-law fits above  $\log_{10}(E/\text{eV}) = 17.5$ . Two twice-broken fits with comparable fit deviances at a lower and higher second break position are reported.

1 1		
	$J(E)_{ m Twice\ Broken}$ , Lower $E_2$	$J(E)_{ m Twice\ Broken}$ , Higher $E_2$
$J(E = 10^{18} \text{ eV}) \times 10^{-30} \text{ eV}^{-1} \text{ m}^{-2} \text{ sr}^{-1} \text{ s}^{-1}$	$2.22 \pm 0.01$	$2.22 \pm 0.01$
$\gamma_1$	$-3.29 \pm 0.01$	$-3.29 \pm 0.01$
$\log_{10}(E_1/\text{eV})$	$18.74 \pm 0.03$	$18.72 \pm 0.05$
$\gamma_2$	$-2.62 \pm 0.06$	$-2.70 \pm 0.05$
$\log_{10}(E_2/\text{eV})$	$19.46 \pm 0.10$	$19.83 \pm 0.04$
$\gamma_3$	$-3.77 \pm 0.41$	$-8.04 \pm 2.74$
D <sub>Poisson</sub> /ndf	22.69/24	23.29/24

**Table 12** Monocular combined spectrum thrice-broken power law fits above  $\log_{10}(E/eV) = 17.5$ .

	$J(E)_{ m Thrice\ Broken}$
$J(E = 10^{18} \text{ eV}) \times 10^{-30} \text{ eV}^{-1} \text{ m}^{-2} \text{ sr}^{-1} \text{ s}^{-1}$	$2.23 \pm 0.01$
$\gamma_1$	$-3.29 \pm 0.01$
$\log_{10}(E_1/\text{eV})$	$18.78 \pm 0.04$
$\gamma_2$	$-2.49 \pm 0.15$
$\log_{10}(E_2/\text{eV})$	$19.20 \pm 0.11$
$\gamma_3$	$-3.04 \pm 0.19$
$\log_{10}(E_3/\text{eV})$	$19.850 \pm 0.001$
$\gamma_4$	$-7.74 \pm 2.43$
D <sub>Poisson</sub> /ndf	17.74/22

 $3.37 \times 10^{-5}$  which gives a  $4.15\sigma$  significance. Measuring the energy at which the flux has been reduced by half of what it would have been with no break [40], the  $\log_{10}(E_{1/2}/\text{eV})$  for the higher second break twice-broken fit was determined to be  $19.77 \pm 0.04$  which is consistent with previous measurements from spectra in the northern hemisphere.

#### 7. The TA-HiRes monocular combined result

To further increase the statistics of this 10-year result, we combine the result with the previous HiRes-I and -II FD experimental results. We justify combining these results with the following points: the experiments use the same event reconstruction methods; the experiments use similar FD detector designs; both experiments use MC-simulated events to understand the reconstruction resolution and to determine the aperture; the location of the HiRes Experiment at Dugway Proving Grounds is not far from Delta, UT, thus both experiments see very similar portions of the night sky.

The data used from HiRes-I and HiRes-II came in the format of events list from Douglas Bergman (private communication) used to

Table 13
TA-HiRes Monocular combined once broken power law fit results.

	$J(E)_{ m Once\ Broken}$
$J(E = 10^{18} \text{ eV}) \times 10^{-30} \text{ eV}^{-1} \text{ m}^{-2} \text{ sr}^{-1} \text{ s}^{-1}$	$2.22 \pm 0.01$
$\gamma_1$	$-3.28 \pm 0.01$
$\log_{10}(E_1/\text{eV})$	$18.64 \pm 0.03$
$\gamma_2$	$-2.85 \pm 0.03$
D <sub>Poisson</sub> /ndf	70.36/31

**Table 14**TA-HiRes Monocular combined twice broken power law fit results. Two twice-broken fits with comparable fit deviances at a lower and higher second break position are reported.

	$J(E)_{ m Twice\ Broken}$ Lower $E_2$	$J(E)_{ m Twice\ Broken}$ , Higher $E_2$
$J(E = 10^{18} \text{ eV}) \times 10^{-30} \text{ eV}^{-1} \text{ m}^{-2} \text{ sr}^{-1} \text{ s}^{-1}$	$2.200 \pm 0.003$	$2.200 \pm 0.003$
$\gamma_1$	$-3.28 \pm 0.01$	$-3.28 \pm 0.01$
$\log_{10}(E_1/\text{eV})$	$18.70 \pm 0.03$	$18.68 \pm 0.03$
$\gamma_2$	$-2.69 \pm 0.04$	$-2.76 \pm 0.03$
$\log_{10}(E_2/\text{eV})$	$19.50 \pm 0.06$	$19.79 \pm 0.08$
$\gamma_3$	$-3.77 \pm 0.23$	$-5.46 \pm 0.96$
D <sub>Poisson</sub> /ndf	33.35/29	32.40/29

create event distribution and the final published results used for the first observation of the GZK suppression for HiRes-I and HiRes-II exposures [7,41]. The results from HiRes span over 1997/05/30–2005/05/13 for HiRes I and 1999/12/01–2004/08/25 for HiRes-II. As with the BR and LR combined result, HiRes-I and HiRes-II have a region of overlap. Given the shortcomings of the event list and absence of the original MC to determine the exposure, we could not determine the overlap region and thus could not fully combine HiRes-I and -II. To get the best statistics, we use HiRes-II for energies  $17.5 \leq \log_{10}(E/\text{eV}) < 18.5$  as HiRes-II went lower in energy and HiRes-I for energies  $\log_{10}(E/\text{eV}) \geq 18.5$  as HiRes-I had greater exposure and thus more high energy events.

The TA-HiRes monocular combined event distribution is shown in Fig. 17, and the TA-HiRes monocular combined exposure is shown in Fig. 18. The spectrum from the TA-HiRes monocular combined result is shown in Fig. 19. The same spectrum is shown in comparison to the TA combined ICRC 2019 [15] spectrum and the Pierre Auger combined ICRC 2019 [42] spectrum in Fig. 20. As was done with the TA monocular combined result, the TA-HiRes monocular combined result was fit with a series of once, twice, and a thrice broken power laws. The results of the broken power law fits are shown in Fig. 21 and the spectral fit parameter values are given in Tables 13–15.

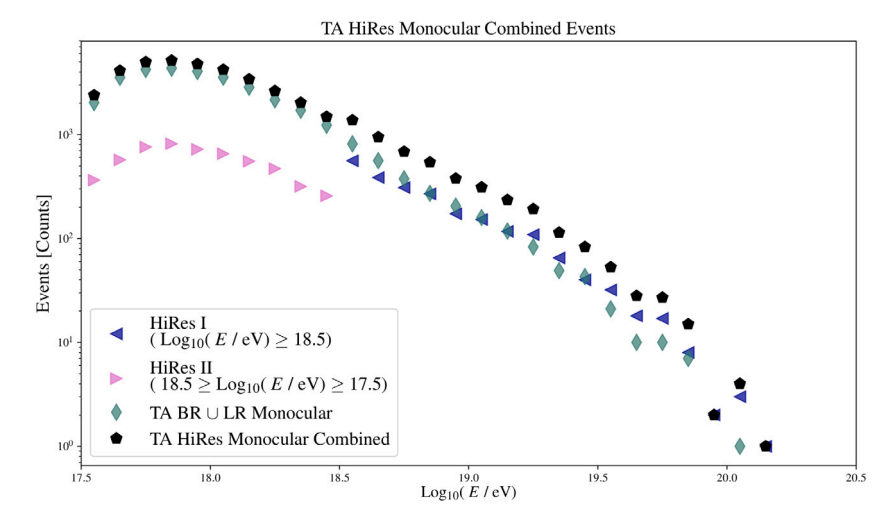


Fig. 17. The combined event distribution for the TA and HiRes monocular results. The HiRes events where combined with the TA BR and LR 10-year monocular results using HiRes-II events for  $17.5 \le \log_{10}(E/\text{eV}) < 18.5$  and HiRes-I events for  $\log_{10}(E/\text{eV}) \ge 18.5$ .

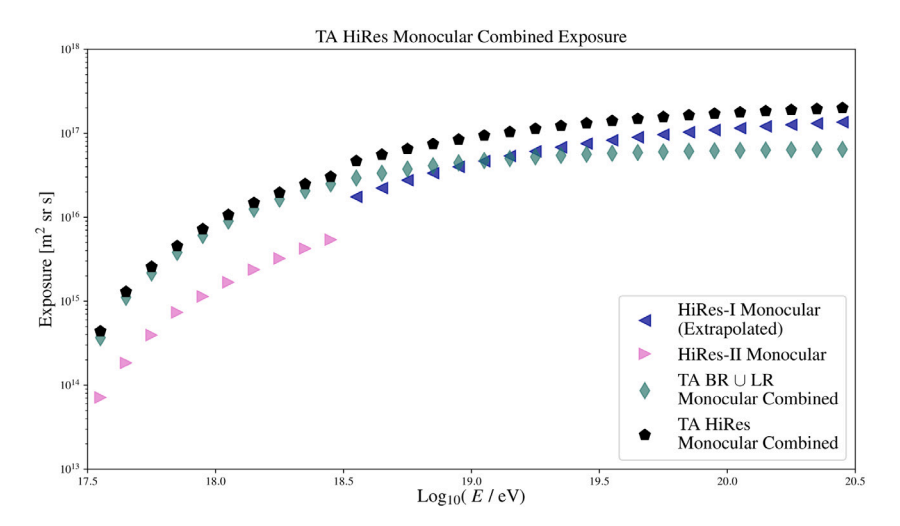


Fig. 18. The combined monocular exposure for the TA and HiRes monocular results. The HiRes exposures where combined with the TA BR and LR 10-year monocular results using HiRes-II exposure for  $17.5 \le \log_{10}(E/eV) < 18.5$  and HiRes-I exposure for  $\log_{10}(E/eV) \ge 18.5$ .

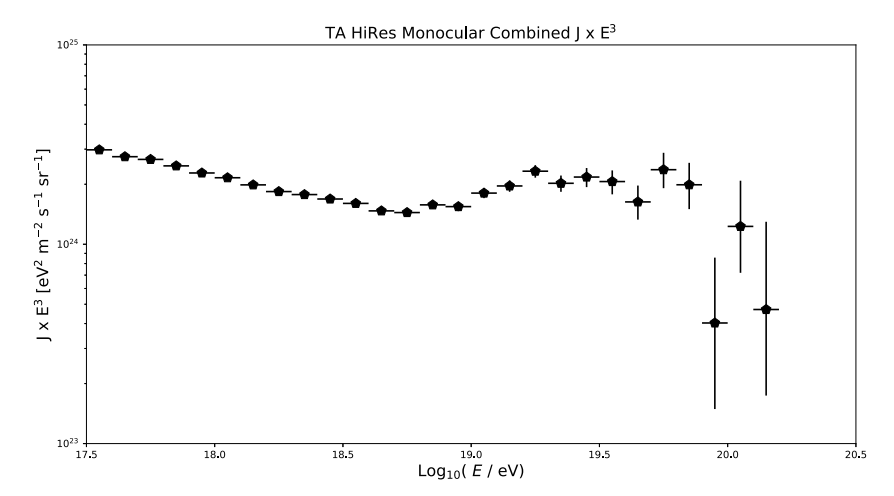


Fig. 19. The combined spectrum for the TA and HiRes monocular results.

Again we see two comparable deviance per degrees of freedom twice broken fits, but the one with a higher second break is again comparable to previous results. The thrice-broken fit has a significant

decrease in deviance per degrees-of-freedom compared to the once- and twice-broken fits. This again suggests another break beside the ankle feature and the high-energy suppression at  $\log_{10}(E/\text{eV}) \approx 19.25$ . This

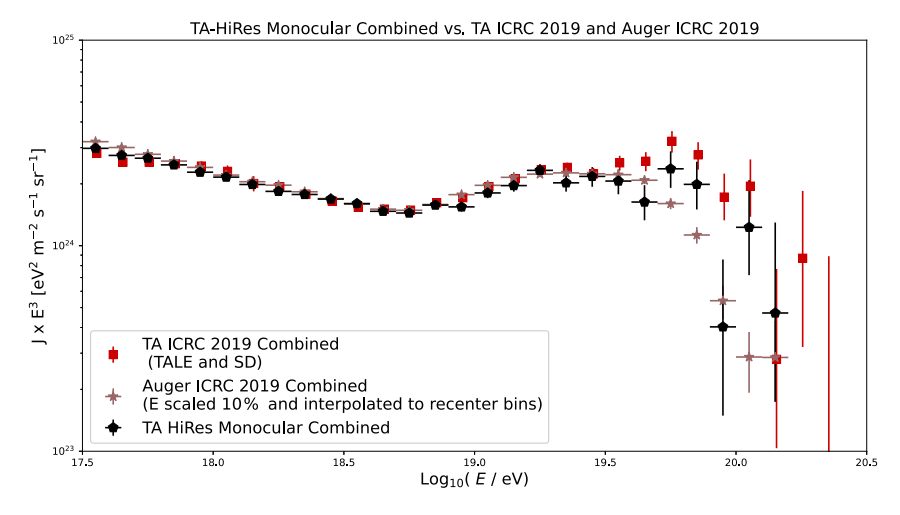


Fig. 20. The TA-HiRes combined monocular spectrum compared to the TA spectrum presented at the 2019 ICRC [15] and the Pierre Auger spectrum presented at the 2019 ICRC [42].

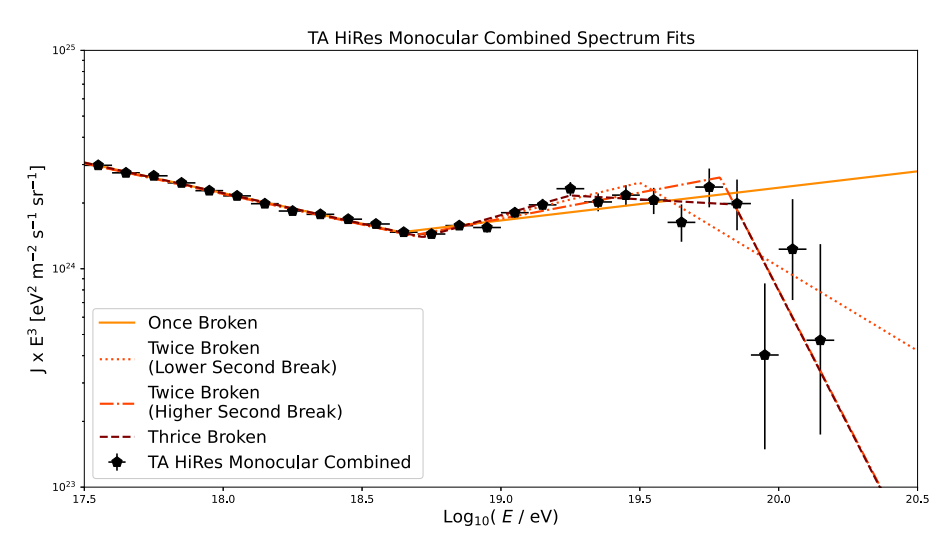


Fig. 21. Broken fits to the combined spectrum for the TA and HiRes monocular results.

Table 15
TA-HiRes Monocular combined thrice broken power law fit results.

R.U. Abbasi et al.

	$J(E)_{\text{Thrice Broken}}$
$J(E = 10^{18} \text{ eV}) \times 10^{-30} \text{ eV}^{-1} \text{ m}^{-2} \text{ sr}^{-1} \text{ s}^{-1}$	$2.22 \pm 0.01$
$\gamma_1$	$-3.28 \pm 0.01$
$\log_{10}(E_1/\text{eV})$	$18.72 \pm 0.02$
$\gamma_2$	$-2.64 \pm 0.05$
$\log_{10}(E_2/\text{eV})$	$19.25 \pm 0.01$
$\gamma_3$	$-3.07 \pm 0.11$
$\log_{10}(E_3/\text{eV})$	$19.84 \pm 0.05$
$\gamma_4$	$-5.47 \pm 0.98$
D <sub>Poisson</sub> /ndf	20.02/27

feature is also suggested by results from the Auger in the southern hemisphere [11]. We should note that the Auger results do not support the interpretation of the high energy suppression being the result of the GZK process [10].

We determined the spectral break significances for the TA HiRes monocular combined result. For the high-energy suppression at  $\log_{10}\left(E_2\right)$  eV ) = 19.79  $\pm$  0.08 for the higher second break twice broken, we expect 66.24 events but only observe 22 events. The twice-broken fit, used to calculate the expected vs. observed events for the high-energy suppression, is shown in Fig. 22(a). This corresponds to a Poisson chance probability of 2.61  $\times$  10 $^{-10}$  or 6.32 $\sigma$  significance. The

 $\log_{10}(E_{1/2}/\text{eV})$  for the higher second break twice-broken fit is calculated to be 19.75  $\pm$  0.08.

We also calculate the significance of the second break and the high-energy suppression simultaneously using the thrice-broken fit and calculating the Poisson probability given the events expected if the spectrum continued unbroken at the breakpoint vs the events observed after the breakpoint. The thrice-broken fit used to calculate the expected vs. observed events for the high-energy suppression is shown in Fig. 22(b). We expect 562.49 events between the second and third break (19.2  $\leq \log_{10}(E/\mathrm{eV}) \leq 19.8$ ) and observe 497. Thus we observe the second break feature with a 2.65  $\times$  10<sup>-3</sup> Poisson chance probability of  $3.01\sigma$  significance. Past the third break, attributed to the high-energy suppression in the thrice-broken fit, we expect 41.39 events and observe 22 events. We observe the high-energy suppression with  $2.64\times10^{-3}$  Poisson chance probability or  $3.38\sigma$ . We calculate  $\log_{10}(E_{1/2}/\mathrm{eV})=19.82\pm0.07$  when including both breaks beyond the ankle.

#### 8. Discussion and conclusion

We observe the high-energy suppression with a significance above  $4\sigma$  using the TA monocular combined spectrum. The improvement in the Poisson deviance per degrees-of-freedom for the thrice-broken fit suggests another break between the ankle and the high-energy

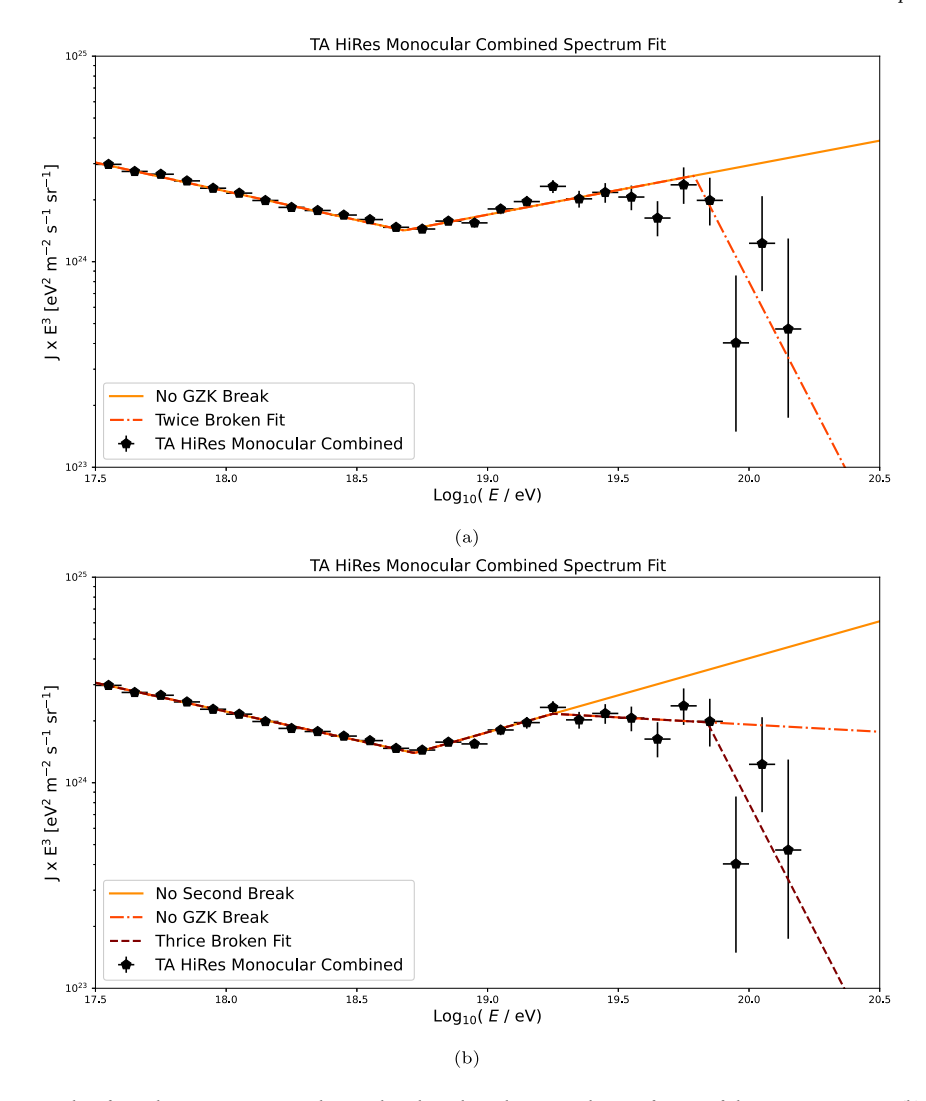


Fig. 22. (a): The twice-broken power law fit to the TA-HiRes monocular Combined result to determine the significance of the GZK suppression. (b): The thrice broken power law fit to the TA HiRes monocular Combined result to determine the significance of the new break feature around  $\log_{10}(E/\text{eV}) \approx 19.25$  and the GZK suppression simultaneously.

suppression. This suggestion of a new break has also been observed in the southern hemisphere by the Pierre Auger cosmic ray observatory [11]. The inclusion of the third fluorescence detector station, MD, which is built of refurbished HiRes FDs in this analysis would increase the event statistics significantly. However because of differences in instrumentation and analysis, MD spectrum data was not incorporated at this time.

The TA-HiRes monocular combined result has the highest highenergy suppression significance, above  $6\sigma$ , ever reported using the fluorescence detection method. We also performed the first calculation of both spectral features above the ankle using a thrice broken fit. We observed both features with a significance above  $3\sigma$ . We attribute the drop from  $6\sigma$  to  $3\sigma$  in the significance of the high-energy suppression to the decrease in the spectral slope after the second break in the thricebroken fit compared to the spectral slope before the second break in the twice-broken fit. This decreases the number of expected events thus decreasing the significance. However, we consider the twice-broken fit result as a valid method for observation of the high-energy suppression. The high-energy suppression is the most apparent break beyond the ankle and thus confirmed first. At this point, we do not claim an observation of a spectral break at  $\log_{10}(E/\mathrm{eV})\approx19.25$  using this data. The  $E_{1/2}$  values determined from the TA HiRes monocular combined result are consistent with previous results from the northern hemisphere, an observation of the GZK suppression, and with propagation models for protonic sources at the highest energy level.

#### **Declaration of competing interest**

The authors declare the following financial interests/personal relationships which may be considered as potential competing interests: Douglas R. Bergman reports financial support was provided by National Science Foundation.

#### Data availability

The authors do not have permission to share data.

#### Acknowledgments

The Telescope Array experiment is supported by the Japan Society for the Promotion of Science(JSPS) through Grants-in-Aid for Priority Area 431, for Specially Promoted Research JP21000002, for Scientific Research (S) JP19104006, for Specially Promoted Research JP15H05693, for Scientific Research (S) JP19H05607, for Scientific Research (S) JP15H05741, for Science Research (A) JP18H03705, for Young Scientists (A) JPH26707011, and for Fostering Joint International Research (B) JP19KK0074, by the joint research program of the Institute for Cosmic Ray Research (ICRR), The University of Tokyo; by the Pioneering Program of RIKEN for the Evolution of Matter in the Universe (r-EMU); by the U.S. National Science Foundation awards

PHY-1806797, PHY-2012934, PHY-2112904, PHY-2209583, and PHY-2209584 as well as AGS-1613260, AGS-1844306, and AGS-2112709; by the National Research Foundation of Korea (2017K1A4A3015188, 2020R1A2C1008230, & 2020R1A2C2102800); by the Ministry of Science and Higher Education of the Russian Federation under the contract 075-15-2020-778, IISN project No. 4.4501.18, by the Belgian Science Policy under IUAP VII/37 (ULB), by National Science Centre in Poland grant 2020/37/B/ST9/01821. This work was partially supported by the grants of The joint research program of the Institute for Space-Earth Environmental Research, Nagoya University and Inter-University Research Program of the Institute for Cosmic Ray Research of University of Tokyo. The foundations of Dr. Ezekiel R. and Edna Wattis Dumke, Willard L. Eccles, and George S. and Dolores Doré Eccles all helped with generous donations. The State of Utah supported the project through its Economic Development Board, and the University of Utah through the Office of the Vice President for Research. The experimental site became available through the cooperation of the Utah School and Institutional Trust Lands Administration (SITLA), U.S. Bureau of Land Management (BLM), and the U.S. Air Force. We appreciate the assistance of the State of Utah and Fillmore offices of the BLM in crafting the Plan of Development for the site. We thank Patrick A. Shea who assisted the collaboration with much valuable advice and provided support for the collaboration's efforts. The people and the officials of Millard County, Utah have been a source of steadfast and warm support for our work which we greatly appreciate. We are indebted to the Millard County Road Department for their efforts to maintain and clear the roads which get us to our sites. We gratefully acknowledge the contribution from the technical staffs of our home institutions. An allocation of computing resources from the Center for High Performance Computing at the University of Utah as well as the Academia Sinica Grid Computing Center (ASGC) is gratefully acknowledged.

#### References

- [1] D.J. Bird, et al., Detection of a cosmic ray with measured energy well beyond the expected spectral cutoff due to cosmic microwave radiation, Astrophys. J. 441 (1995) 144–150.
- [2] K. Greisen, End to the cosmic ray spectrum? Phys. Rev. Lett. 16 (1966) 748–750.
- [3] G.T. Zatsepin, V.A. Kuzmin, Upper limit of the spectrum of cosmic rays, JETP Lett. 4 (1966) 78-80.
- [4] H. Kawai, et al., Telescope Array experiment, Nucl. Phys. B 175–176 (2008) 221–226.
- [5] T. Abu-Zayyad, et al., The prototype high-resolution Fly's Eye cosmic ray detector, Nucl. Instrum. Methods A 450 (2000) 253–269.
- [6] N. Chiba, et al., Akeno giant air shower array (AGASA) covering 100-km\*\*2 area, Nucl. Instrum. Methods A 311 (1992) 338–349.
- [7] R.U. Abbasi, et al., First observation of the Greisen–Zatsepin–Kuzmin suppression, Phys. Rev. Lett. 100 (2008) 101101.
- [8] J. Abraham, et al., Observation of the suppression of the flux of cosmic rays above  $4\times10^{19}$  eV, Phys. Rev. Lett. 101 (2008) 061101.
- [9] T. Abu-Zayyad, et al., The cosmic ray energy spectrum observed with the surface detector of the Telescope Array experiment, Astrophys. J. Lett. 768 (2013) L1.
- [10] A. Aab, et al., Features of the energy spectrum of cosmic rays above 2.5×10<sup>18</sup> eV using the Pierre Auger Observatory, Phys. Rev. Lett. 125 (12) (2020) 121106.
- [11] A. Aab, et al., Measurement of the cosmic-ray energy spectrum above 2.5×10<sup>18</sup> eV using the Pierre Auger Observatory, Phys. Rev. D 102 (6) (2020) 062005.
- [12] A. Aab, et al., Combined fit of spectrum and composition data as measured by the Pierre Auger Observatory, J. Cosmol. Astropart. Phys. 04 (2017) 038; Erratum, JCAP 03 (2018) E02.
- [13] T. Abu-Zayyad, et al., The energy spectrum of ultra-high-energy cosmic rays measured by the Telescope Array FADC fluorescence detectors in monocular mode, Astropart. Phys. 48 (2013) 16–24.
- [14] R.U. Abbasi, et al., The energy spectrum of cosmic rays above 10<sup>17,2</sup> eV measured by the fluorescence detectors of the Telescope Array experiment in seven years, Astropart. Phys. 80 (2016) 131–140.

- [15] D. Ivanov, Energy spectrum measured by the Telescope Array, PoS ICRC2019 (2020) 298.
- [16] H. Tokuno, et al., New air fluorescence detectors employed in the Telescope Array experiment, Nucl. Instrum. Methods A 676 (2012) 54–65.
- [17] Y. Tameda, et al., Trigger electronics of the new fluorescence detectors of the telescope array experiment, Nucl. Instrum. Methods A 609 (2009) 227–234.
- [18] S. Kawana, et al., Calibration of photomultiplier tubes for the fluorescence detector of Telescope Array experiment using a Rayleigh scattered laser beam, Nucl. Instrum. Methods A 681 (2012) 68–77.
- [19] B.K. Shin, et al., Gain monitoring of telescope array photomultiplier cameras for the first 4 years of operation, Nucl. Instrum. Methods A 768 (2014) 96–103.
- [20] P. Sokolsky, G.B. Thomson, Highest energy cosmic rays and results from the HiRes experiment, J. Phys. G 34 (2007) R401.
- [21] R.M. Baltrusaitis, G.L. Cassiday, R. Cooper, B.R. Dawson, J.W. Elbert, B.E. Fick, D.F. Liebing, E.C. Loh, P. Sokolsky, D. Steck, The Fly's Eye detector: Present and future, Nucl. Instrum. Methods A 264 (1988) 87–92.
- [22] DOC/NOAA/NWS/NCEP/EMC Environmental Modeling Center, National Centers for Environmental Prediction, Global Data Assimilation System (GDAS), NOAA National Centers for Environmental Information (NCEI), 2001.
- [23] F. Kakimoto, E.C. Loh, M. Nagano, H. Okuno, M. Teshima, S. Ueno, A measurement of the air fluorescence yield, Nucl. Instrum. Methods A 372 (1996) 527–533.
- [24] R. Abbasi, et al., Techniques of the FLASH thin target experiment, Nucl. Instrum. Methods A 597 (2008) 32–36.
- [25] R. Abbasi, et al., The FLASH thick-target experiment, Nucl. Instrum. Methods A 597 (2008) 37–40.
- [26] T.K. Gaisser, A.M. Hillas, Reliability of the method of constant intensity cuts for reconstructing the average development of vertical showers, in: Proceedings of the 15th International Cosmic Ray Conference, Plovdiv, Vol. 8, ICRC, 1977, pp. 353–357.
- [27] F. Nerling, J. Bluemer, R. Engel, M. Risse, Universality of electron distributions in high-energy air showers: Description of Cherenkov light production, Astropart. Phys. 24 (2006) 421–437.
- [28] T. Abu-Zayyad, et al., Evidence for changing of cosmic ray composition between 10\*\*17-eV and 10\*\*18-eV from multicomponent measurements, Phys. Rev. Lett. 84 (2000) 4276–4279.
- [29] R.U. Abbasi, et al., Indications of proton-dominated cosmic ray composition above 1.6 EeV, Phys. Rev. Lett. 104 (2010) 161101.
- [30] A. Aab, et al., Data-driven estimation of the invisible energy of cosmic ray showers with the Pierre Auger Observatory, Phys. Rev. D 100 (8) (2019) 082003.
- [31] T. Fujii, M. Fukushima, D. Ikeda, D. Ivanov, J.P. Lundquist, B. Shin, G. Thomson, Y. Tsunesada, A systematic uncertainty on the energy scale of the Telescope Array fluorescence detectors, PoS ICRC2017 (2018) 524.
- [32] G.D. Furlich, Observation of the GZK Suppression with the Telescope Array Fluorescence Telescopes and Deployment of the Telescope Array Expansion (Ph.D. thesis), University of Utah, 2020.
- [33] United States. National Oceanic and Atmospheric Administration and United States. National Aeronautics and Space Administration and United States Committee on Extension to the Standard Atmosphere and United States. Department of the Air Force, U.S. Standard Atmosphere, 1976, in: NOAA SIT 76-1562, National Oceanic and Amospheric [sic] Administration, 1976.
- [34] D. Heck, J. Knapp, J.N. Capdevielle, G. Schatz, T. Thouw, CORSIKA: A Monte Carlo code to simulate extensive air showers, 1998.
- [35] D. Ivanov, TA spectrum summary, PoS ICRC2015 (2016) 349.
- [36] S. Hochreiter, J. Schmidhuber, Long short-term memory, Neural Comput. 9 (8) (1997) 1735–1780.
- [37] S. Baker, R.D. Cousins, Clarification of the use of chi square and likelihood functions in fits to histograms, Nucl. Instrum. Methods 221 (1984) 437–442.
- [38] R.L. Workman, et al., Review of particle physics, PTEP 2022 (2022) 083C01.
- [39] W. Cash, Parameter estimation in astronomy through application of the likelihood ratio, Astrophys. J. 228 (1979) 939–947.
- [40] V. Berezinsky, A.Z. Gazizov, S.I. Grigorieva, Dip in UHECR spectrum as signature of proton interaction with CMB, Phys. Lett. B 612 (2005) 147–153.
- [41] D.R. Bergman, HiRes spectra and integral spectra, 2007, http://www.physics.rutgers.edu/dbergman/HiRes-Monocular-Spectra-200702.html. URL is now inactive, results provided by Douglas Bergman via private communication.
- [42] V. Verzi, Measurement of the energy spectrum of ultra-high energy cosmic rays using the Pierre Auger observatory, PoS ICRC2019 (2020) 450.